

Alma Mater Studiorum Università di Bologna
Archivio istituzionale della ricerca

Geomorphic process signatures reshaping sub-humid Mediterranean badlands: 2. Application to 5-year dataset

This is the final peer-reviewed author's accepted manuscript (postprint) of the following publication:

Published Version:

Llena M., Smith M.W., Wheaton J.M., Vericat D. (2020). Geomorphic process signatures reshaping sub-humid Mediterranean badlands: 2. Application to 5-year dataset. *EARTH SURFACE PROCESSES AND LANDFORMS*, 45(5), 1292-1310 [10.1002/esp.4822].

Availability:

This version is available at: <https://hdl.handle.net/11585/737693> since: 2020-02-27

Published:

DOI: <http://doi.org/10.1002/esp.4822>

Terms of use:

Some rights reserved. The terms and conditions for the reuse of this version of the manuscript are specified in the publishing policy. For all terms of use and more information see the publisher's website.

This item was downloaded from IRIS Università di Bologna (<https://cris.unibo.it/>).
When citing, please refer to the published version.

(Article begins on next page)

This is the final peer-reviewed accepted manuscript of:

Llena, M., Smith, M.W., Wheaton, J.M., Vericat, D., Geomorphic process signatures reshaping sub-humid Mediterranean badlands: 2. Application to 5-year dataset (2020) *Earth Surface Processes and Landforms*, 45 (5), pp. 1292-1310

The final published version is available online at <https://doi.org/10.1002/esp.4822>

Terms of use:

Some rights reserved. The terms and conditions for the reuse of this version of the manuscript are specified in the publishing policy. For all terms of use and more information see the publisher's website.

This item was downloaded from IRIS Università di Bologna (<https://cris.unibo.it/>)

When citing, please refer to the published version.

Llena Manel (Orcid ID: 0000-0001-7095-6188)

Smith Mark (Orcid ID: 0000-0003-4361-9527)

Wheaton Joseph (Orcid ID: 0000-0002-8361-8150)

Geomorphic process signatures reshaping sub-humid Mediterranean badlands: 2. Application to 5 years dataset

Llena, M.^{1,*}, Smith, M.W.², Wheaton, J.M.³, Vericat, D.^{4,5}

¹ Fluvial Dynamics Research Group, Department of Environment and Soil Sciences, University of Lleida, Lleida, Spain.

² School of Geography, University of Leeds, Leeds, UK.

³ Department of Watershed Sciences, Utah State University, Logan, USA.

⁴ Serra Húnter Fellow, Fluvial Dynamics Research Group, Department of Environment and Soil Sciences, University of Lleida, Lleida, Spain.

⁵ Forest Science and Technology Centre of Catalonia, Solsona, Spain.

* Corresponding author: mllena@macs.udl.cat

Running head: Geomorphic processes in badlands: 2. Application to 5 years dataset

This article has been accepted for publication and undergone full peer review but has not been through the copyediting, typesetting, pagination and proofreading process which may lead to differences between this version and the Version of Record. Please cite this article as doi: 10.1002/esp.4822

Abstract

Badland landscapes exhibit high erosion rates and represent the main source of fine sediments in some catchments. Advances in High Resolution Topographic methods allow analysis of topographic changes at high temporal and spatial scales. We apply the Mapping Geomorphic Processes in the Environment (MaGPiE) algorithm to infer the main geomorphic process signatures operating in two sub-humid badlands with contrasting morphometric attributes located in the Southern Pyrenees. By interrogating a five-year dataset of seasonal and annual topographic changes, we examine the variability of geomorphic processes at multiple temporal scales. The magnitude of geomorphic processes is linked to landform attributes and meteorological variables. Morphometric differences between both adjacent badlands allow analysing the role of landform attributes on main geomorphic process re-shaping landscapes subjected to the same external forcing (i.e. rainfall and temperature).

The dominant geomorphic process signatures observed in both badlands are different, despite their close proximity and same rainfall and temperature regimes. Process signatures determining surface lowering in the gentle-sloping south-facing badland, characterised by lower connectivity and more vegetation cover, are driven by surface runoff-based processes, both diffuse, causing *Sheet Washing*, and concentrated, determining *Cutting and Filling* and *Rilling and Gullying*. The steeper and more connected north-facing slopes of the other badland are re-shaped by means of gravitational processes with *Mass Wasting* dominating topographic changes. In terms of processes determining surface raising, both *Mass Wasting* and *Cutting and Filling* are most frequently observed in both badlands. There is a clear near-balanced feedback between both surface-raising and lowering processes that becomes unbalanced at larger temporal scales due to the thresholds overcoming, as the volume associated with surface lowering becomes higher than that associated with raising-based processes. Rainfall variables control surface flow processes while those variables associated with low temperature have a significant relation with mass movement-based processes and other localised processes as *Regolith Cohesion Loss*. Finally, our results point out as morphometry (slope and connectivity) together with vegetation cover are key factors determining geomorphic processes and associated topographic changes.

Key words: badlands, geomorphic process signatures, morphometry, meteorology, topographic change, MaGPiE algorithm.

1. INTRODUCTION

Badlands are described as dissected landscapes with little or no vegetation cover developed on unconsolidated or poorly consolidated sedimentary deposits (Yair et al., 1980; Clotet et al. 1987; Gallart et al 2002). Badlands are usually subjected to high erosion rates, representing the main source of fine sediments in some catchments (e.g. López-Tarazón et al., 2012; Richard and Mathys 1999). High erosion rates implies high sediment transfer downstream, with associated environmental (e.g. channel clogging, Piqué et al. 2014; alluvial plain dynamics alteration, Aucelli et al., 2016) and management implications (e.g. reservoir siltation, Martínez-Casasnovas and Poch, 1998; reduction of water quality, Pimentel et al., 1995). The significance of geomorphic processes in badlands will be determined, mainly, by their morphometric characteristics, including lithology, together with external forcing (i.e. rainfall and temperature). Moreno-de las Heras and Gallart (2018) proposed three badlands types according to a ratio between the potential evapotranspiration (PET) and the mean annual precipitation (MAP), and based on the original classification of Gallart et al. (2002). They classified (i) Arid badlands ($MAP < 200 \text{ mm}$; $PET/MAP < 0.20$); (ii) Semi-arid and dry sub-humid badlands ($MAP = 200\text{-}700 \text{ mm}$; $PET/MAP = 0.20\text{-}0.65$) and (iii) Sub-humid and Humid badlands ($MAP > 700 \text{ mm}$; $PET/MAP > 0.65$). Those climates with marked seasonal contrasts (i.e. temperature, rainfall) favour the development of badlands. In that way, Mediterranean regions represent one of the areas with the greatest presence of these types of landscapes (Clotet et al., 1987; Torri et al., 1994).

Lithology and its interaction with the characteristics of the climate, vegetation cover, connectivity and human activity are considered the main factors responsible for badland development (Smith 1958; Clotet et al. 1987; Gallart et al. 2002; Nadal-Romero and Garcia-Ruiz 2018). In a general way, the main geomorphic processes that shape badland landscapes and control their spatial and temporal evolution are weathering (i.e. regolith formation), surface flow-based processes (i.e. diffuse or concentrated), subsurface erosion (i.e. piping or tunnelling) and mass-wasting (i.e. gravitational processes) (Bryan and Yair 1982; Clotet et al. 1988; Kananin-Grubin 2013; Moreno-de las Heras and Gallart, 2018).

Erosion rates on badlands are mainly analysed by dynamic or volumetric methods (De Ploey and Grabiels, 1980; Nadal-Romero and García-Ruiz, 2018; Sirvent et al., 1997). On one hand, dynamic methods aim at measuring sediment fluxes from plots (e.g. Nadal-Romero et al., 2007; Regüés et al., 1995), micro-catchments (e.g. Mathys et al., 2003) or experimental catchments (e.g. Rainato et al., 2017). On the other hand, volumetric methods aim at measuring sediment erosion rates through the analysis of topographic changes. Historically, volumetric methods were based on sparse observations across relatively small areas, based on erosion pins (e.g. Barnes et al., 2016; Benito et al., 1992) or microprofile metres (e.g. Descroix and Olivri, 2002; Sirvent et al., 1997).

During recent decades, advances in High Resolution Topographic survey methods (see reviews and examples in e.g. Passalacqua et al., 2015; Tarolli, 2014; Vericat et al., 2017) offer the opportunity of examining topographic changes in a spatially-distributed way at multiple temporal and spatial scales. Several authors have used these data sets to monitor topographic changes in badlands (e.g. Aucelli et al., 2016; Ferrer et al., 2017; Krenz and Kuhn, 2018; Lucia et al., 2011; Nadal-Romero et al., 2015; Nobajas et al., 2017; Smith and Vericat, 2015; Stöcker et al., 2015; Vericat et al., 2014). Although these studies have improved the quantification of erosion and deposition rates, and associated sediment yields, to our knowledge, there has yet to be an attempt to quantify the magnitude of the changes in form associated with the main geomorphic processes, its relation with morphometric characteristics, and their spatial and temporal distribution. Most of the studies are concentrated in relatively small temporal and spatial scales that may limit the applicability of findings beyond the period in which observations are obtained. In this way, for a comprehensive understanding of the drivers and processes reshaping badlands and their role on sediment production, it is necessary to quantify not just topographic changes across these landscapes, but also to infer in the main geomorphic processes being responsible of the changes at multiple temporal and spatial scales.

In this paper we analyse multi-temporal repeat High Resolution Topography obtained during five consecutive years in two morphometrically-contrasted sub-humid badlands to untangle the relative importance of different processes in reshaping badlands and exporting sediments downstream, and their link to landform attributes and meteorological variables. Specifically, we have applied the Mapping Geomorphic Processes in the Environment (MaGPiE) algorithm recently developed by Llana et al. (2020) to infer into main geomorphic process signatures shaping these badlands through the analysis of changes in form. It is worth to mention that this paper together with the mentioned methodological paper (Llana et al., 2020) are considered a paper pair. The methodological paper presents the full details of the MaGPiE algorithm. In this article, however, we have applied the aforementioned algorithm to an extensive long-term dataset (i.e. five years) from two experimental badlands located in the Southern Central Pyrenees that are broadly representative of sub-humid badlands developed in Sub-humid Mediterranean landscapes. The starting hypothesis is that morphometric characteristics will determine in a large degree the typology, extension and magnitude of geomorphic process. For this reason, the two adjacent badlands with contrasted landform attributes but subjected to the same external forcing (i.e. temperature and rainfall) provide an idealised design to analyse the interaction between meteorological variables, landform attributes and main geomorphic process signatures at multiple temporal scales. Better understanding of main geomorphic processes re-shaping badlands, together with their relation with meteorological variables and morphometric characteristics, will help providing information about cycles of sediment

production and their drivers, which could be very useful data to improve environmental management and landscape evolution modelling.

2. STUDY SITE

The study site is composed of two adjacent experimental micro-catchments (i.e. Badland 1 -B1- with a surface area of 0.32 ha, and Badland 2 -B2- with a surface of 0.21 ha) situated in the Soto catchment (Figure 1A); a small (10 km²) intermittent tributary of the Upper River Cinca (8275 km², Central Pyrenees, Ebro Catchment, Iberian Peninsula; Figure 1A). The distance between both micro-catchments is around 50 m. The main land uses of the Soto catchment are forest (56%), badlands (26%) and field crops (18%). Overall, the average altitude of both Badlands is around 600 m a.s.l.; the local relief can be more than 19 m with steep slopes and high degree of dissection (Figure 1A and 1B). In terms of lithology, both experimental badlands are composed by a sequence of Eocene marls with different degrees of bedrock compactness with some alternate layers of sandstones and gypsum. Therefore, geomorphic processes are hypothesised to be highly complex and spatially variable (Smith and Vericat, 2015; Figure 1B). In terms of their specific morphometry (Table 1), differences are mainly controlled by the dip of the geological strata. In this way, B2 presents a higher dip of the strata (i.e. 40°) than B1 (i.e. 25°), that determines, among other characteristics, a higher slope and a major network incision, which in turn controls the degree of structural sediment connectivity (see the geomorphological maps of both badlands in Figure 1 of the Supplementary Materials for further information). Sediment connectivity was estimated by the topographic-based Sediment Connectivity Index modified by Cavalli et al. (2013) and first developed by Borselli et al. (2008). This pixel-based index is computed by on the ratio between an upslope component (i.e. contributing area, roughness and slope) and downslope component (i.e. flow path length, roughness and slope). After its normalization, the Sediment Connectivity Index represents the probability of sediment arriving at each pixel reaching the catchment outlet or a given targeted point. For instance, a low value of the index indicates a lower probability of the sediment reaching the targeted point, while a high value indicates that the pixel is well connected and there is a high probability that sediment reaches the outlet or targeted point (see examples of sediment connectivity maps for both study badlands in Figure 2 of the Supplementary Materials section). The aspect of both badlands is also different, being 211° (i.e. SW) for B1 and 171° (i.e. S) for B2 (Figure 1A and 1B and Table 1). In terms of land cover, the two badlands have a low vegetation cover (i.e. <20%), composed by isolated shrubs (e.g. *Buxus sempervirens*, *Genista scorpius*) in steep slopes and small groups of relatively young trees (e.g. *Pinus halepensis*) on low slopes or in the top of the micro-catchments (Figure 1A). The experimental badland B1 was also

presented in Smith and Vericat (2015). More information about the experimental site can be also obtained in <https://sites.google.com/site/badlandscan/>.

The long-term meteorological background is provided by a meteorological station located 250 m from the study site (i.e. Aínsa Station, Spanish Meteorological Agency, AEMET). Mean annual rainfall for the period 1981-2018 is around 755 mm. Maximum rainfall is observed during spring and autumn (e.g. maximum intensities around 47 mm h⁻¹ are registered). Mean annual temperature is 13°C, with minimum values around -6°C and maximum around 37°C. During winter, temperatures below freezing are often registered (on average, 60 days every year are exposed to temperatures <0°C).

3. METHODS

3.1. Field data collection and preparation

3.1.1. Rainfall & Temperature

Rainfall was measured continuously by a Campbell ARG100 tipping bucket rain gauge, while air temperature was recorded using a Campbell Temperature Probe-109 (see location in Figure 1C). All data were recorded in the same datalogger (Campbell CR200X) at a 5-minute interval. A total of eight meteorological variables were calculated based on the recorded rainfall and temperature (see Table 2 for two for a complete description). Note that the sensors were located in B1; however, the proximity of both badlands (around 50 meters; Figure 1B) together with the minimum changes in elevation between them (Table 1; Figure 1B) justifies the use of a single station to characterise both badlands.

3.1.2. Topographic Surveys and Processing Methods

Topographic data sets were obtained through different High Resolution Topographic survey techniques. The number and frequency of the surveys were variable depending on the experimental badland. In B1, 10 topographic surveys were performed between summer 2013 and summer 2018. From 2013 to 2016, surveys were done annually (n=4), while from 2016 to 2018 surveys were done seasonally (n=6; Table 3 and Figure 2). In the case of B2, the surveyed period was between autumn

2016 and summer 2018, with all the surveys at a seasonal interval ($n=5$; Table 3 and Figure 2). Note that, all the annual surveys were performed in the middle of the summer to ensure that the annual scale is defined by two consecutive summer surveys (e.g. 2017-2018). In the case of the seasonal surveys, these were performed during the middle of summer, at the end of the autumn and at the beginning of the spring (see Figure 3 in Supplementary Materials section for further information about the survey periods). These surveys yield the following seasonal periods: (i) spring (beginning spring to middle summer; e.g. S2017), (ii) autumn (middle summer to end autumn; e.g. A2017) and (iii) winter (end autumn to beginning spring; e.g. W2017). We selected these periods in order to isolate the potential effects of meteorological drivers (e.g. rainstorms in spring and summer, and temperatures below 0°C in winter) on weathering and erosion processes. Finally, it is worth noting that the year attributed to every period is always the starting year (e.g. the winter between 2017 and 2018 is named W2017; Table 4).

Topographic surveys were performed by means of: (i) Terrestrial Laser Scanning (TLS); and (ii) Structure from Motion (SfM) photogrammetry. Note that TLS surveys were only performed in B1 during Survey 1 (S01) and Survey 2 (S02); all other surveys were performed by SfM photogrammetry in both badlands (Table 3).

Specifically, the TLS surveys were performed by a Leica ScanStation C10. The C10 uses a 532-nm pulsed laser with stated precisions of 6 mm for position, 4 mm for distance, and 60 μ rad for angles. The maximum data acquisition rate is 50000 points per second while the maximum survey range is 300 m. B1 was surveyed using the same 12 stations in each survey chosen to minimize and eliminate gaps caused by occlusion. Further specific details are provided in Smith and Vericat (2015). In terms of the SfM-based surveys, around 650 pictures per campaign and badland were taken by means of a Panasonic Lumix DMC-TZ60 compact camera (focal length 4 mm which is a 35-mm equivalent of 25 mm; 10 Mpx) mounted on a 10 m telescopic inspection pole. SfM processing was implemented using standard workflows within Agisoft Photoscan Professional 1.3.4. Dense point clouds with an average point density of around 5×10^4 obs m^{-2} (i.e. 5 obs cm^{-2}) were obtained. In terms of georeferencing and scaling, TLS data sets were registered by a floating network of tripod-mounted targets (i.e. 6" circular blue/white targets) used as Ground Control Points (GCPs). SfM data sets were registered by a floating control network of around 30 GCPs per badland, which were spatially distributed. Both GCPs sets were surveyed with a Leica TPS1200 Total Station (TS). The TS was set up based on a primary control network of four (fixed) benchmarks. The coordinates in each benchmark were obtained by means of a Leica Viva GS15 GNSS system and RINEX data from 3 reference stations. Data quality of the primary

control network (3D quality, i.e. horizontal and vertical) was 0.006 m on average, with a standard deviation of 0.0017 m.

In terms of quality assessment, an independent validation dataset of around 300 Check Points (ChPs) per survey was obtained with the TS. The corresponding differences between ChPs and TLS or SfM-derived point cloud were calculated by the M3C2 plugin implemented in the open source software CloudCompare 2.6.2. M3C2 computes the local distance between two point clouds along the normal surface direction, which tracks 3D variations in surface orientation (Lague et al., 2013). The validation metrics used to analyse the differences in terms of quality were the Mean Absolute Error (i.e. MAE) as a measure of the accuracy, and the Standard Deviation of the differences (i.e. SDE) as a measure of the precision (as previously by e.g. Greenwalt and Schultz, 1968; Westaway et al., 2003; Williams et al., 2014; Mosbrucker et al., 2017).

Point clouds were filtered to remove outliers and vegetation. Outliers were filtered by means the Statistical Outlier Filter (SOR) of Cloud Compare 2.6.2 (Girardeau-Montaut, 2016), while the points located in vegetated areas were removed using the combination of the results of the supervised image classification (in case of the SfM-based surveys) and also manually (TLS-based surveys). After that, the open-source Topographic Point Cloud Analysis Toolkit (ToPCAT; Brasington et al., 2012; Rychkov et al., 2012; implemented in the Geomorphic Change Detection extension for ArcMap, available at <http://gcd.joewheaton.org/>; see Wheaton et al. 2010) was used to regularize the point cloud. A 0.05 x 0.05 m grid was selected taking into account the magnitude of the topographic changes of the study area and the size of the smallest geomorphic features observed in the field (e.g. rills). ToPCAT further allows interrogation and analysis of observations within each grid cell. A series of cell-based statistics were calculated (e.g. maximum, mean and minimum elevations and detrended standard deviation of elevations). The minimum elevation within each grid was used to represent the ground elevation within each cell, while the detrended standard deviation was used as a proxy of surface roughness as previously used by, for instance, Brasington et al. (2012), Smith and Vericat (2015) and Vericat et al. (2014). A Triangular Irregular Network or TIN was calculated based on these observations for each survey. Finally, a 0.05 m resolution DEM and roughness map was computed from each TIN.

3.2. Data analyses

3.2.1. Geomorphic Change Detection

Figure 3 shows the general workflow applied to analyse topographic changes. Topographic changes were estimated by means of the comparison of DEMs between surveys (DEM of Differencing; i.e.

DoD). The old DEM is subtracted from the new one, where negative values indicate surface lowering or erosion, and positive values indicate surface raising or deposition. DoDs were calculated by the Geomorphic Change Detection 7.2 (GCD) extension for ArcMap (Wheaton et al. 2010). GCD also allows adding uncertainty analysis based on simple minimum Level of Detection (minLoD), propagated errors or probabilistic thresholding. Given the relatively low magnitude of the expected topographic changes in the study area compared with other landscapes (e.g. gravel-bed rivers), a robust approach for the estimation of these changes was necessary to discriminate the real changes from noise. In that way, the three steps proposed by Wheaton et al. (2010) were applied to assess DoD uncertainty: (i) quantifying spatially distributed uncertainty for each DEM; (ii) propagating identified uncertainties into each DoD; and (iii) determining the significance of the propagated uncertainty based on a minimum Level of Detection (minLoD). The assessment of the spatially distributed uncertainty was addressed by the application of a Fuzzy Inference System (FIS) to consider errors from different sources (Wheaton et al., 2010). In this study we have used the FIS model proposed by Rossi (2018). This model takes into account the slope and the roughness as main factors determining the vertical uncertainty. Roughness and slope were categorised based on four different levels: low, moderate, high and extreme. These were combined to determine 4 levels of uncertainty (see Figure 4 of Supplementary Materials section for additional information). The values defining or associated to these 4 levels were adapted to the study site by Llena et al. (2018), which range from 0.02 to 1 m of surface error on average. A critical t-value at a confidence interval of 85% was applied to calculate the spatially distributed minLoD (e.g. Brasington et al., 2000; Lane et al., 2003; Smith and Vericat, 2015). Those DoD cells with absolute values below the minLoD were considered uncertain and not used in the computation of the thresholded DoD (Figure 5 of Supplementary Materials section shows the spatial distribution of the minLoD for both study badlands).

3.2.2. Geomorphic Process Signatures

The Mapping Geomorphic Processes in the Environment (MaGPiE) algorithm presented by Llena et al. (2020) was used to infer on the main geomorphic process signatures controlling topographic changes. Here we present a summary of the MaGPiE but additional details can be found in Llena et al. (2020).

Main geomorphic process signatures were grouped into: (i) weathering-based processes, (ii) water-based (surface) processes, and (iii) mass movement-related processes (following Barnes et al., 2016; Bryan and Yair, 1982; Clotet et al., 1987; Gallart et al., 2002; Nadal-Romero and Regües, 2010; Nadal-Romero and García-Ruiz, 2018; Moreno-de las Heras and Gallart, 2018; Vergari et al., 2019). According to these, a total of a total of 6 specific geomorphic process signatures were identified: (1) *Sheet Washing*; (2) *Rilling and Gullying*; (3) *Cutting and Filling*; (4) *Mass Wasting* (5) *Regolith Cohesion Loss*;

and (6) *Overlapping Processes*. It is worth mentioning that sub-surface geomorphic processes (i.e. pipping) were not taken into account here because these are not acting in the experimental badlands. However, changes in form associated with these processes may be dominant in other environments (e.g. Faulkner, 2018; Gutiérrez et al. 1997), requiring consideration in the identification of main geomorphic process signatures in such environments.

Briefly, the algorithm allows pixel-based identification of the specific geomorphic process signatures by the combination of (i) landform attributes (i.e. Slope, Roughness and a new Concentrated Runoff Index) and (ii) topographic changes, represented by the results of the thresholded DoD. The landform attributes were extracted from the second (or most recent) DEM (see Figure 3 for the general workflow). The local Slope was calculated by means of the maximum rate of change in elevation from each cell to its neighbours. The Roughness was calculated using ToPCAT-derived detrended standard deviation of the elevations in each grid cell (0.05 m). The Concentrated Runoff Index (i.e. CRI) was calculated based on the Topographic Wetness Index (TWI) and Planform Curvature (PC) by means of the expression $TWI + (PC \times -1)$; where the TWI was computed as $\ln(A/\tan\beta)$, A is referred to the upslope area of a given cell (m^2), and β is the local gradient (in degrees). PC represents the normalised (from -1 to 1) planform curvature value obtained from the most recent DEM (see more details in Llena et al., 2020). Finally, topographic changes were obtained by the comparison of the DEMs between surveys as described above (i.e. thresholded DoD). To define the signature of each process, each attribute and the DoD was grouped into different classes. An expert-map of the main geomorphic process signatures was created in order to (a) establish the thresholds of the classes of each attribute and DoD and define the signatures (i.e. combination of classes; using 90% of the expert-map results) of each geomorphic process, and (b) to validate the accuracy of the classification (using the remaining 10% of the expert-map).

Each landform attribute was divided in two classes: high and low in case of roughness and slope; or diffuse flow and concentrated flow in case of the Concentrated Runoff Index. DoD values are divided into four classes: high lowering, low lowering, low raising and high raising. The thresholds of each class and their combinations are based on the distribution of the values of the landform attributes and DoD per each geomorphic process. In the case of the landform attributes, the median value of each attribute was calculated across the whole DEM. These values will determine the class boundaries. In order to assign each geomorphic process signature to a class, the median value of the same attribute for cells classified into each geomorphic process is then compared with the class ranges and categorised accordingly (see example in Figure 1). In case of the thresholds for the DoD values, 0 defines the division between surface lowering and raising classes, while the 90th and 10th percentiles of the DoD values define the thresholds between high and low raising and lowering, respectively.

Again, once the thresholds were established, the median DoD values in each process were analysed to classify each process. The combination of these classes provides a unique signature or combination per each process. For instance, the signature that defines surface lowering caused by *Rilling and Gullying* is: High Slope, High or Low values of Roughness, Concentrated Flow (High CRI) and either High or Low surface lowering. Therefore, a pixel that has all these inputs will be characterised as lowering potentially caused by *Rilling and Gullying*. It is worth noting that in our case we have considered *Overlapping Processes* those yielding a distinct signature to the other identified processes, mainly, in the particular case of our badlands, *Sheet Washing and Regolith Cohesion Loss*. For more details about the class boundaries and combinations identified for each geomorphic process see Llena et al. (2020).

Once the thresholds of the classes of all inputs were defined, the classified rasters were combined in a multiband raster: a single data set in which each pixel has associated the different combinations of the input data sets. The signatures of each process were then considered to classify the multiband raster. In order to automate the processes and repeat it in subsequent analyses, a supervised Maximum Likelihood Image Classification was performed. First, a training sample for each process is created and a signature file for the whole training samples was saved. This signature file can be considered valid for mapping geomorphic processes in badlands based on the specific mentioned process signatures, and the thresholds defined per each class of the input data sets.

As a proxy of the accuracy of the classification, 100 random points were distributed per each study period along the study area. The classification results in these points based on the expert-map (observed processes) were compared with the MaGPiE results by a confusion matrix calculated following the method described by Chuvieco (2016). This comparison allows assessing the percentage agreement of the method. Finally, the thresholded DoDs were segmented based on each geomorphic process through the GCD ArcMap-based extension (Figure 3). This last step allows the assessment of areal, vertical and volumetric changes associated to each process and for each study period (see more specific details in Llena et al., 2020).

3.2.3. Statistical analysis

The role of the meteorological variables on the geomorphic processes and associated topographic changes was analysed by means of Pearson correlation coefficients. A p-value of 0.05 was established to consider the correlations statistically significant.

4. RESULTS

4.1. Quality assessment

4.1.1. Topographic data sets

Registration and georeferencing

TLS-based surveys (i.e. S01 and S02) presented a registration error (3d) of 0.31 cm and 0.27 cm respectively. Both point clouds had an average point density larger than 6.7 points cm⁻². As mentioned above, the SfM-based surveys (i.e. S03-S11) were georeferenced by means of around 30 floating GCPs per badland. Table 3 shows the different Georeferencing Errors associated with each SfM-derived point cloud. Reported 3d errors range from 1.80 cm to 4.11 cm, with an average error of 2.32 cm. The highest errors were observed in the surveys S05 (i.e. 3.52 cm) and S06 (i.e. 4.11 cm) of the B2, and were mainly due to problems caused by the poor image overlapping in some areas. These problems were corrected in the following surveys, decreasing the errors to values smaller than the average (Table 3). The average point density of SfM-based ranged between 5 and 10 points cm⁻².

Point cloud validation

All the point clouds were independently validated by the ChPs surveyed by the TS, except S01 in which no ChPs were obtained. Results are presented in Table 3. The average MAE (i.e. 1.93 cm) is slightly smaller than the average SDE (2.52 cm) but with the same range, indicating that surveys have similar accuracy and precision. B2 presented, on average, higher MAE and SDE, especially in S05 (i.e. MAE of 2.49 cm and SDE of 3.27 cm) and S06 (i.e. MAE of 3.48 cm and SDE of 3.98 cm). As mentioned above, high errors in these surveys could have been due to the limited overlapping between photographs in some areas.

Both methods (TLS and SfM-based) were used in S03 in B1 to assess the differences between them (see more details in Llena et al., 2018). Briefly, a total of 4 patches (around 5 m²) were selected. These patches were considered representative of flat surfaces, steep slopes, and high and low surface roughness for both micro-catchments. Both TLS and SfM-based point clouds in these patches were compared. Results indicated a MAE of 0.64 cm and a SDE of 0.71 cm, concluding that the differences between methods would not have a direct impact on the analyses of topographic changes.

4.1.2. Geomorphic process signatures maps

Overall, the average percentage of agreement of the MaGPie classification is 77 % for B1 and 73 % for B2 (Table 3). In B1, the highest accuracy was obtained in S06 (i.e. 84 %) and the lowest in S07 (i.e. 62%), while in B2 the highest was obtained in S08 (i.e. 85%) and the lowest in S07 (i.e. 64%). The classification agreement (i.e. CA %) values for the three surveys showing the highest GE, MAE and SDE

errors (surveys S05, S06 and S07 with CA ranging 64-68%) is notably poorer than for the other three listed surveys (S08, S09 and S10 with CA 73-85%), which also show better data quality. In terms of the accuracy per each class, in B1 the most reliable signature is *Regolith Cohesion Loss* (86 % of agreement) with *Sheet Washing* signatures being the most challenging to identify (63 % of agreement). In B2 the most reliable signature is *Rilling and Gullying* (i.e. 85 % of agreement), while *Mass Wasting* (67 % of agreement) and *Cutting and Filling* (66 % of agreement) are identified least readily.

4.2. Meteorological characterization of the periods

Main meteorological variables calculated for all the surveyed periods are presented in Table 4 and Figure 2. Annual average rainfall was 818 mm, ranging from 657 mm registered during 2015-2016, to 1001 mm registered in 2017-2018 (Table 4). According to the long-term data (1981-2018) from a nearby station (as stated in the study area section), we consider 2015-2016 as a dry year (i.e. -12 % of the mean long-term rainfall, i.e. 755 mm), while 2017-2018 can be categorised a wet year (i.e. +32% of the long-term mean). The lowest rainfall intensities (i.e. *MRI* and *MaxRI*) were registered during the wettest periods (i.e. 2016-2017 and 2017-2018). Contrary, highest intensities were registered in the driest periods (i.e. 2014-2015 and 2015-2016; Table 4). In terms of temperature, as for the total rainfall, the annual periods in which the highest number of days in which the temperature was below 0°C were registered were 2016-2017 and 2017-2018 (i.e. 109 and 86 days respectively); while 2014-2015 and 2015-2016 presented fewer days with temperature below 0°C (i.e. 49 and 31 days respectively). The magnitude of the minimum temperatures was associated with the number of days in which temperatures below 0°C were registered. Both the minimum temperature and number of days below 0°C were lower and larger respectively in 2016-2017 and 2017-2018.

Results also indicate a high seasonal variability. Maximum rainfall was registered in Spring 2018 (S2018), while the highest intensity was observed in S2017, the driest season in the study period. The number of days with temperature below 0°C in each season was highly variable, ranging from 102 in W2017 to none in A2017. Although W2017 was the season with more days below freezing, W2016 was the coldest season with an average below 0°C temperature of -3.28 °C, and a minimum temperature of -9.89 °C (see Table 4 and Figure 2 for more details).

4.3. Topographic Changes

Table 5 presents the DoD results for both badlands and for the different study periods. Figure 4 and Figure 5 show the DoD maps of representative areas in each badland. The magnified representative areas are presented to facilitate the visualization and interpretation of the results. Maps of the entire badlands are provided in Figures 6 and 7 of the Supplementary Materials. It should be noted that negative and positive DoD values do not imply always erosion and sedimentation processes. For instance, a positive value of the DoD could reflect elevation increases due to both sedimentation or surface swelling; while a negative value may reflect surface lowering due to erosional or shrink processes. Therefore, to avoid confusion, we consider that red colours indicate surface lowering while blue represent surface raising.

Overall, the areas presenting topographical changes above the minLoD (i.e. >0.02 m on average) were relatively small, indicating that the magnitude of topographic changes was relatively low and in the range of the uncertainty of the surveys. Topographic changes were spatially and temporally concentrated; intermittent high magnitude changes were observed over the five-year dataset. These observations indicate that although significant changes are only observed in less than a 5% of the total area (on average for all surveys), surface raising and lowering in these areas may be significant, up to 10 cm of change. Surface lowering was mainly located in high slope areas and in the main channels (see examples in Figures 4 and 5); yet, surface raising was mainly observed in the accumulation zones located at the toe of the slopes near the main channels, and also in the main channels themselves (Figures 4 and 5). These patterns are observed at all temporal scales, annually and seasonally, and in both badlands, B1 and B2. Finally, in terms of the areal changes, our results indicate that both areas associated with surface lowering and those with surface raising are relatively more widespread in the seasonal analyses compared with annual observations.

Annually, net changes ranged between virtually none (i.e. 0.01 cm yr^{-1}) in 2014-2015 to -0.15 cm yr^{-1} in 2013-14 (yielding a maximum net export of -3.86 m^3). A similarly high value to the latter was also observed in 2016-17 (i.e. -0.13 yr^{-1} , $-3.34 \text{ m}^3 \text{ yr}^{-1}$). Net changes near or above -1 cm were observed at temporal scales larger than the annual (Table 5). The net change observed in B1 for the period 2016-18 was -0.86 cm (-4.31 m^3), a larger value compared to the net change in B2 for the same period (i.e. -0.22 cm or -2.26 m^3 , values yielding annual values of -0.11 cm yr^{-1} or $-1.13 \text{ m}^3 \text{ yr}^{-1}$). Long term topographic changes observed in B1 (2013-18) yielded a net change of -4.09 cm (-0.8 cm yr^{-1} , -4.18 m^3

yr⁻¹). Differences in mean annual net changes based on the length of the period analysed indicate processes that are heavily variable through time and, consequently, values may be highly biased based on the period used to study topographic changes. Additionally, changes can be highly variable spatially too. Seasonally, net topographic changes are very low; the largest value was observed in B2 in A2017 (i.e. -0.11 cm). The largest volumetric change was observed in B1 in S2008 (-2.41 m³). The sign of the net change fluctuates between positive and negative values. All the periods with positive net values of change presented relatively very low values, with the exception of the winter seasons where positive net changes are higher (Table 5). It is worth noting that values obtained for short temporal scales (seasonal and annual) do not add up to longer term values when compared. For example, net change observed in B1 for the period 2016-18 (i.e. 0.86 cm) yielded an average annual net change of -0.43 cm yr⁻¹, but the average value of net changes assessed based on the annual scale observations was -0.08 cm yr⁻¹. In B2, for the same period, annual changes oscillate between -0.11 cm yr⁻¹ and -0.02 cm yr⁻¹, depending on the temporal scales used to estimate the mean annual change. These differences are attributed to the effect of the minLoD. Areas subjected to changes below the minLoD (i.e. uncertain changes) are generally more extensive when a shorter survey interval is analysed. In terms of differences between badlands, Figure 6 shows that as the total changes observed in B2 are between 2 and 4 times higher than the computed for B1. In general, both volumes attributed to surface lowering and raising are always higher in B2 than in B1. Additionally, the seasonal evolution of the specific net changes show that dominant processes are variable in space.

In terms of the relation between the magnitude of change and surveyed time span, Figure 7 shows topographic changes (i.e. Lowering, Raising, Net Topographic Change and Total Topographic Change) observed at different temporal scales in each badland. When temporal scales are smaller than one year (i.e. seasonal), both badlands did not present a clear trend, presenting net changes around zero, while negative net changes are obtained at longer temporal scales.

4.4. Geomorphic process signatures

Figure 8 shows the distribution of each geomorphic process signature identified by the MaGPiE algorithm. Although results indicate that signatures are variable through time, the main signatures observed during the study period are: *Cutting and Filling* in B1 and *Mass Wasting* in B2. Information about area occupied by each geomorphic processes in both experimental badlands and both temporal scales (i.e. annual and seasonal) is presented in Figure 8 of the Supplementary Materials. In particular,

the process observed over the largest area was *Cutting and Filling* during the annual scale 2016-17 in B1 (i.e. 31 m²); specifically, 42 % of the area above the minLoD for this period was attributed to this process signature. In both badlands, the geomorphic process signature observed with lower magnitude, both in terms of volume and area, was *Overlapping Processes*. It is worth noting that this process signature is attributed when an observed topographic change cannot be attributed to any other process classification. As such, the overlapping processes class may also include other processes not identified or selected as the main geomorphic process signatures.

Figure 8A and 8B show the volume of change attributed to each process signature together with the evolution of the volumetric net change for all the study periods and for B1 and B2, respectively. Main surface lowering-based processes responsible for the volumetric changes observed in B1 were those driven by surface runoff either diffuse (e.g. *Sheet Washing*) or concentrated (e.g. *Rilling and Gullying*, *Cutting and Filling*). *Sheet Washing* occurred in less steep but highly exposed slopes (e.g. ii in Figure 9). Erosion caused by *Rilling and Gullying* was observed in steep slopes perpendicular to main channels (e.g. i in Figure 10), while *Cutting and Filling* occurred in the main channel bottoms (i and iii in Figure 10). The main lowering-based process observed in B2 was *Mass Wasting*, although, occasionally, processes driven by surface runoff also caused high magnitude changes (e.g. S2018). Erosion caused by *Mass Wasting* were mainly observed in the steepest north-face slopes (e.g. iii in Figure 9 and i and ii in Figure 10) and triggered by gravitational processes together with rainsplash erosion, mobilising the regolith that was previously weathered by freeze-thaw and soil moisture changes (e.g. Barnes et al., 2016).

In relation to surface raising-based process signatures, deposition caused by *Mass Wasting* is the principal process observed in both badlands for all time scales, followed by *Cutting and Filling* and *Regolith Cohesion Loss* in the case of B1, and *Rilling and Gullying* in B2. Deposition caused by *Mass Wasting* was mainly observed in the bottom of the main channels, associated with the fallen regolith coming from steep slopes (e.g. iii in Figure 9 and ii in Figure 10), or with small accumulation zones located at the base of the slopes near the main channel (e.g. ii in Figure 10). In the latter case, gelivation processes and rainsplash erosion in the slopes are considered to be the main drivers (e.g. Nadal-Romero and Regüés, 2010). The magnitude of these process signatures was generally low and, consequently, likely below the minLoD and thus not mapped. The magnitude of deposition caused by *Mass Wasting* trends to be larger, mainly due to both the accumulation of materials in small areas and the increase of the volume of the regolith after its fracture (e.g. iii in Figure 9; Nadal-Romero et al.,

2007); consequently, these process signatures are less biased and clearly observed in the map. Deposition caused by *Rilling and Gullying* had a relatively low magnitude, especially in B1; mainly due to the low stability of regolith sedimentation deposits in steep slopes (i.e. where mainly rills and gullies are developed). Finally, *Regolith Cohesion Loss* was one of the surface-raising processes that yielded lower volumetric changes, especially in B2. Surface rising associated to this process is mostly due to the fracture of the regolith caused by both the freeze-thaw (e.g. Barnes et al., 2016; Tsutsumi and Fujita, 2016) and moisture-change cycles (e.g. Nadal-Romero and Regüés, 2010). The main location of this process is in flat and north slopes (shaded areas; e.g. i in Figure 9). Figures 9 and 10 only show some examples of geomorphic maps of process signatures linked to field observations for different periods in some specific areas; the entire geomorphic maps are presented in Figure 9 and 10 of the Supplementary Materials.

4.5. Statistical correlations between meteorological variables and geomorphic processes

Table 6 show the results of the Pearson correlation matrix between topographic changes segmented by the main geomorphic process and the meteorological variables. Rainfall variables are well correlated with lowering processes driven by surface flow. For instance, *In-channel Erosion* is significantly correlated with Rainfall Duration (*RD*) in B1, and *Rill and Gully Erosion* is correlated with Total Rainfall (*TR*) and *RD* in B2. Variables associated with minimum temperatures are significantly correlated with *Regolith Fall Erosion* in the two badlands (i.e. days with temperatures lower than 0° - *Zd*- in B1, and minimum temperature -*MinTZD*- in B2). In B2, surface raising processes such as *Rill and Gully Deposition* are correlated with *Zd*, while *In-channel Deposition* is significantly correlated with mean temperature (*MT*) and *Zd*. Our results also indicated that *Regolith Cohesion Loss* is significantly correlated with the mean temperature of days below 0°C (*MTZD*) in B2. Finally, *Overlapping Processes* are not correlated with any of the measured meteorological variables.

Overall, geomorphic process observed in B1 presented better correlations with rainfall-based variables, while those observed in B2 presented better correlations with the variables related to minimum temperatures. This is verified when the results for the total change are observed (Table 6). For instance, a significant positive correlation between total topographic change and Maximum Rainfall Intensity (*MRI*) is observed in B1, while, in B2, total topographic change is significantly correlated with the number of days below 0°C (i.e. *Zd*) and the mean temperature of the minimum temperatures of the days below 0°C (i.e. *MTZD*).

5. DISCUSSION

5.1. The role of meteorological variables on geomorphic processes

Several authors have observed correlations between erosional processes and rainfall events such as the ones observed in this study. Canton et al. (2000) described how, in arid badlands of SE Spain, main erosive processes were driven by high-intensity rainfall events, while in nearby badlands, Solé-Benet et al. (2012) observed as erosional processes and rainfall intensity were more correlated than with the total rainfall. Desir and Marín (2013) observed, in a badland located in the NE of Spain with similar characteristics to our study area, that erosional processes were mainly controlled by both the amount of rainfall and its intensity. Although the method used to assess erosion differs to our approach (i.e. sparse observations versus continuous spatial distributed erosion and sedimentation values), their results are in agreement to our observations.

Correlations between variables associated with minimum temperatures and *Regolith Fall Erosion* for both badlands are in agreement with those reported by Barnes et al. (2016), who concluded that mass wasting processes produced in sidewalls (i.e. *Mass Wasting* in our study) are mainly controlled by freeze-thaw events in a scarcely vegetated area of the East of the USA. Although a substantial volume of the materials mobilised by *Mass Wasting Erosion* is deposited in the toe of the slopes, a large proportion of these materials is transported by surface flows and finally deposited in the main channels of the badlands. These interactions may explain the significant correlation between variables associated with minimum temperatures and depositional processes in channels in B2; and were also observed by Descroix and Olivry (2002), who noted that runoff caused by rainfall events mobilize the regolith previously weathered by freeze-thaw cycles in the Black marls of Draix (Southern Alps, France). At the same time, the significant correlation between *Regolith Cohesion Loss* and the mean temperature of the minimum temperatures of the days below 0°C (*MTZD*) in B2, indicates that *Regolith Cohesion Loss* is probably mainly controlled by freeze-thaw cycles. Nadal-Romero and Regüés (2010) observed that, in sub-humid badlands developed on marls (Central Pyrenees, NE Iberian Peninsula, Spain), maximum regolith alteration was produced during winter periods, mainly due to the freeze-thaw cycles that caused the so-called *popcorn* morphology. As stated, weathered surfaces will be the main source of sediments during subsequent rainfall events. In this way, Regüés et al. (1995) also proved that the main erosional processes in badlands of the eastern Pyrenees (NE Iberian Peninsula, Spain), were controlled by weathering, freeze-thaw cycles, and that these materials were depleted from the slopes after rainfall events.

Generally, geomorphic process observed in B1 presented better correlations with rainfall-based variables, while those observed in B2 presented better correlations with the variables related to minimum temperatures. Due to the fact that the meteorological variables are the same in both badlands, differences between correlations may be explained by the existence of other controlling factors such as, for instance, the morphometry of the badlands (see details in Table 1).

5.2. The role of morphometry on geomorphic processes

As presented in Section 4.4., the contribution of the main geomorphic processes signatures in each badland to sediment transfer and export was slightly different. In terms of surface lowering-based processes, B1 mainly demonstrated processes driven by surface runoff, both diffuse (i.e. *Sheet Washing*) and concentrated (i.e. *Cutting and Filling*, *Rilling and Gullyng*). In B2 *Mass Wasting* were the main observed processes. The MaGPIE algorithm permitted the mapping of geomorphic processes based on the magnitude and sign of the topographic changes and several variables related to the morphometry of the badlands. The significance of surface-runoff based processes in B1 can be partly explained by the larger catchment area compared to B2 (i.e. around 30% more; Table 1), meaning that B1 potentially has a greater propensity toward runoff concentration than B2 due to its relatively higher upslope catchment areas. In the badlands of the Mocatán catchment (Southeast Spain), Faulkner et al. (2008) stated that incision in the main channels increased hydraulic gradients upstream, reconnecting channels with slopes and encouraging gullies development on side slopes. In the case of the B2, however, there are higher slopes (i.e. 16% more than B1; Table 1). The local slope is one of the main parameters that determine stability, and consequently, has a direct control on triggering mass movements (i.e. *Mass Wasting*; Bishop and Morgenstern, 1960; Morgenstern and Price, 1965). Additionally, several authors have pointed out that the aspect is, together with the slope, one of the main factors determining geomorphic processes since they have a direct control on freeze-thaw and dry-wet cycles which are active regolith-weathering agents in shady aspects (e.g. Yair et al. 1980; Calvo-Cases and Harvey, 1996; Nadal-Romero et al. 2007; Vericat et al., 2014; Nadal-Romero et al. 2015). Mean slope on shady aspects in B2 is 31% higher than in B1, proving an explanation as to why *Mass Wasting* processes are higher than in B1.

In terms of surface raising-based processes, *Mass Wasting* is the main geomorphic process observed in both badlands. Even so, the magnitude of change for this process was higher in B2. This difference can be explained by the higher slopes in B2 compared to B1 (Table 1) as stated above. *Mass Wasting* is followed by *Cutting and Filling* processes in both badlands, presenting approximately the same magnitude in terms of surface raising. The third main raising-based process signature differs in each badland: *Regolith Cohesion Loss* in B1 and *Rilling and Gullyng* in B2. High slopes in B2 determined the

accumulations of sediments in the lower parts of rills and gullies. High slopes also favour the instability of the regolith after its fracture (e.g. gelivation process), causing the dislodgment to the lower parts (i.e. *Mass Wasting*). In areas with low slope (e.g. B1), the fractured regolith remains stable and could present popcorn morphologies (i.e. *Regolith Cohesion Loss*).

As discussed, morphometry determines both the typology of the dominant geomorphic process and the magnitude of these, although the absolute magnitude of these is, of course, influenced by the extension of the badlands too. As observed in Table 2, the surface area of both badlands is different; B2 is 62.5% smaller than B1. Specific seasonal (2016-2018) volumetric changes (i.e. $\text{m}^3 \text{ha}^{-1}$) were computed to compare the magnitude of the topographic changes through time in the two badlands. Total changes observed in B2 are between 2 and 4 times higher than the obtained for B1 (Figure 6). Differences between badlands may be attributed to the slope and aspect, as discussed previously, but also to the differences in terms of vegetation cover and sediment connectivity. Broadly, B2 has a lower vegetation cover and higher sediment connectivity than B1 (Table 1). Different studies have focused on the role of vegetation cover preventing erosion in badlands (e.g. Regüés et al., 2000; Gallart et al., 2002; Gallart et al., 2013; Nadal-Romero et al. 2014; Torri et al., 2018). In the Biancana badlands (south of Italy), Torri et al. (2018) observed that the presence of vegetation controls soil properties and the resistance to erosion and degradation. In terms of sediment connectivity, several authors have analysed the feedbacks between badland morphology its evolution, and sediment connectivity (e.g. Faulkner, 2008; Grenfell et al., 2012; Marchamalo et al., 2016). For instance, in semi-arid badlands located in SE Spain, Marchamalo et al. (2016) noted that a high degree of connectivity had a positive and direct relation to the frequency of water and sediment fluxes and, consequently, to slope erosion. In the case of the Mediterranean climate badlands located in South Africa, Grenfell et al. (2012) observed that floodout features exercise control on the severity of erosion, as they prevent the lateral expansion of gullies into badlands.

Finally, it is worth mentioning that lithology also plays an important role on the geomorphic processes reshaping badlands. Lithology determines key physical characteristics of badlands landscapes (e.g. hardness, density) and, consequently, has a direct effect on the potential degree of erosion of these materials. For instance, Cerdá (1997) analysed erosion on badlands developed on two different lithologies, marls and clays, and under the same rainfall conditions. He showed that erosion on marls was two orders of magnitude higher than in clays. At the same time, the lithological typology and the structure of geological features (e.g. dip and strike) has also an influence on the morphometry (Table 1) which, in turn, as seen above, determines the typology of the dominant geomorphological process. Our study area is a clear example of how the geological structure controls badland landscape morphometry and associated geomorphic processes. Regarding the effect of lithology on

morphometry, Moreno-de las Heras and Gallart (2016) observed in the eastern Pyrenees (NE Iberian Peninsula, Spain) how badlands developed on weathering-resistant Eocene marls presented preferential distribution on north-slope aspects, where bedrock gelivation is more intense, and on higher slope angles than badlands developed on swelling and highly unstable (smectite-rich) Garumnian lutites, which did not reveal a clear slope-aspect pattern in the same region. The degree of bedrock compactness of the marl outcrops in the experimental badlands region is relatively high, which, added to the intercalation of hard layers of sandstones and gypsum, means that the badlands of the study area have a relatively low degree of erosion in comparison with other studies in the same region. For instance, Vericat et al. (2014) reported annual net changes of around 6 cm in a small (90 m²) experimental badland located in a nearby catchment with no vegetation cover. Meanwhile, Francke et al. (2008) reported a minimum mean erosion value of 2.1 cm y⁻¹ in the same study area measured by spatially distributed erosion pins. Also in a nearby badlands developed on Eocene marls, Nadal-Romero et al. (2015) observed a mean annual erosion value that range from 0.2 to 7 cm depending on the aspect and survey technique. The differences between these studies and the results reported here may be attributed to the extent over which data were obtained, the method used to acquire the data (punctual observations versus spatially distribute observations), the precision and accuracy of the measurements and the temporal scale in which observations were obtained (as discussed previously). Despite these differences, the experimental badlands can be considered representative, specifically, of all the south face of the Pyrenees' badlands developed on Eocene marls. In a broader sense, they are also representative of badlands developed on these type of materials in sub-humid mountain areas worldwide.

5.3. The role of the temporal scale on depicting main geomorphic processes

As observed in Table 5 and previously stated in other studies (e.g. Balasch et al., 1988; Descroix and Olivry, 2002; Nadal-Romero et al., 2007; Vericat et al., 2014; Aucelli et al., 2016; Ballesteros-Cánovas et al., 2017), topographic changes are sensitive to the temporal scale over which they are computed. This, although self-evident, will influence our understanding of the main geomorphic processes reshaping badlands at longer temporal scales. Thus, having a continuity of five years of study, allows to observe certain patterns in the geomorphic processes, which are not possible with shorter study periods. Geomorphic processes are acting at different temporal scales, driven by meteorological variables and also by other internal factors such as morphometry and lithology, and also conditioned by the effects of the minLoD on the computation of the thresholded DoDs as discussed above. Within this context, processes observed to dominate during winter months may not be the principal agents

of change at annual scales, but nevertheless, may have a direct influence on the preparation of the sediments that eventually will be exported from badlands (at larger temporal scales, e.g. annually). In the same way, results observed during short periods of time may be biased, representing neither the general trend of these landscapes nor gross erosion rates. This is evident when net changes are positive or near zero; a larger temporal scale is required to investigate the net export of sediment. Taking the results of short temporal scales to predict long term patterns would bias the interpretations. In summary, short term surveys capture real changes that might be later masked by compensatory changes acting at longer temporal scales; however, they suffer from the minLoD filtering out small changes, a problem less of an issue over longer timescales.

As stated above, when temporal scales are smaller than one year (i.e. seasonal), both badlands do not present a clear trend in terms of topographic change, presenting net changes around zero (Figure 7). Vericat et al. (2014) analysed the importance of the temporal scale on the analysis of the topographic changes, concluding that although event scale changes are heavily variable, from net surface raising to net lowering, a significant negative pattern (surface lowering, i.e. net export) is observed at the annual scale. Therefore, they suggested the need of appropriately-scaled spatial and temporal data to understand topographic changes and their drivers in badlands.

Increasing the temporal scale to periods of at least one year increases the magnitude of changes, especially in terms of lowering, total and net change (Figure 7). This pattern is observed in both badlands: despite the differences in size and morphometry (Table 1), the average time required to export the sediments weathered and eroded from the slopes is around 1 year, even the geomorphic processes acting in the slopes may differ in time and space. Is worth noting that this time will depend on the magnitude of the assigned minLoD, a fact that reinforces the need to calculate this parameter in the most rigorous possible way. Our observations, in terms of the average time required for that the sediment be depleted from badlands are in agreement with the study of Descroix and Olivry (2002) in the badlands of Draix (South Alps, France), in which they noted that the detached material weathered in the slopes during winter was not completely exported from the catchment until the spring and autumn rainfall. In the case of the badlands of the Vallcebre area (Eastern Pyrenees), several studies (e.g. Gallart et al., 2013; Moreno-de las Heras et al., 2018) also stated similar responses. Our observations demonstrate that surveys at seasonal temporal scales allow depiction of specific geomorphological processes preparing and detaching sediments from the slopes, while annual temporal scales are required to estimate average values of erosion (i.e. denudation), masking the geomorphic processes responsible of long-term changes.

5.4. Limitations and further work

Repeated High Resolution Topography obtained by means of TLS and SfM photogrammetry was used to study topographic changes across multiple temporal scales in two sub-humid Mediterranean badlands. Errors in topographic surveys propagate into uncertainties in the estimates of topographic change (i.e. changes cannot be considered real, e.g. Brasington et al., 2000; Lane et al., 2003; Wheaton et al., 2010), and may also have an indirect impact on the interpretation of geomorphic process signatures. These uncertainties may be relevant in landscapes or over temporal scales in which the change is relatively low compared to the potential errors subjected to the surveys, such as our experimental badlands. In order to depicting real topographic changes from noise, we have applied a thresholding to the DoDs (see section 3.2.1. for further information).

Even so, the use of different error and thresholding propagation methods may yield different results in our estimates since the number of cells above or below the minLoD would change, affecting the computation of topographic changes in both signs. Although our method is widely used in the literature (e.g. Brasington et al., 2000; Lane et al., 2003; Milan et al., 2011; Wheaton et al. 2010), Anderson (2018) has recently demonstrated that net changes estimated from repeat high density observations may be affected by correlated or fully systematic errors and uncorrelated or random errors. He concluded that any attempt to remove these errors may cause a misinterpretation of the results. The same author argued that thresholding (i.e. applying a minLoD) may be a biased correction tool for the estimates of total erosion, total sedimentation and total topographic change. Net changes will be less affected by random errors since errors of opposite sign tend to offset each other, but may be largely affected by correlated or systematic errors (e.g. survey method, Anderson, 2018). In our case, we were not able to correct such systematic errors. Although the comparison of both survey methods provided very close results indicating systematic errors in both would be similar, we are not able to quantify the degree in which such errors (if present) may affect the magnitude of the net changes, especially at the shortest temporal scales analysed.

Our results indicate that High Resolution Topography obtained at different temporal scales (i.e. annual and seasonal) during five consecutive years allows analysis of the relations between main geomorphic processes reshaping badlands and their role on sediment production and transfer. As far as we aware, there are no previous studies analysing topographic changes in badlands at the spatial and temporal resolutions analysed here. Data provided from natural laboratories such as the one presented here (<https://sites.google.com/site/badlandscan/>) are also fundamental to study long-term changes in relation to the frequency and magnitude of rainfall events and future trends in a context of global change.

6. CONCLUSIONS

This paper analyses multi-temporal repeat High Resolution Topography obtained during five consecutive years in two morphometrically-contrasted but adjacent badlands subjected to the same external forcing to untangle the relative importance of different geomorphic processes in reshaping badlands and exporting sediments downstream. The main conclusions are:

1. Both experimental badlands are subjected to low erosion rates (between 0.07 and 0.01 cm/yr on average in B1 and B2 respectively) in comparison with badlands developed on the same lithology in the southern Pyrenees where annual erosion rates can be up to 3 cm/yr. We hypothesise that these differences may be attributed to the size of the experimental badlands, the method used to monitor topographic changes and the higher degree of bedrock compactness, which entails highly complex and spatially variable processes.
2. The dominant geomorphic process signatures observed in both badlands are different. Process signatures determining surface lowering in the gentle-sloping south-facing badland (B1), characterised by lower connectivity and more vegetation cover, are driven by surface runoff-based processes, both diffuse, causing *Sheet Washing*, and concentrated, determining *Cutting and Filling* and *Rilling and Gullying*. The steepest and more connected north-facing slopes of B2 are re-shaped by means of gravitational processes, with *Mass Wasting* being dominant. In terms of processes determining surface raising, both *Mass Wasting* and *Cutting and Filling* are considered the main in both badlands.
3. There is a clear near-balanced feedback between both surface-raising and lowering processes, that gets unbalanced at larger temporal scales, as the volume associated with surface lowering becomes higher than that associated to raising-based processes, indicating that the time required to export the sediments that are weathered and detached from the slopes is around 1 year. This time will depend on the magnitude of the assigned minLoD, a fact that reinforces the need to calculate this parameter in the most rigorous and consistent possible way.
4. Rainfall variables control surface flow processes while those variables associated with low temperature have a significant relation with mass movement-based processes and other localised processes as *Regolith Cohesion Loss*.
5. Morphometry is a key factor that determine geomorphic processes and associated topographic changes. Our results suggest that slope, connectivity and vegetation cover have a direct impact in triggering determinate geomorphic processes.
6. Geomorphic processes are acting at different temporal and spatial scales, driven by meteorological variables and also by other internal factors such as morphometry and lithology. We demonstrated

that seasonal temporal scales are optimum for analysing specific geomorphic processes preparing and detaching sediments from the slopes and these are spatially different; conversely, annual temporal scales are required to estimate average values of erosion (i.e. denudation), diverging to similar gross estimates but masking the short-term geomorphic processes responsible of long-term changes.

Better understanding of main geomorphic processes together with their relation with meteorological variables and morphometric characteristics as the results presented here can be very useful data to improve environmental management and landscape evolution modelling.

Acknowledgements

This research was carried out within the framework of two research projects funded by the Spanish Ministry of Economy and Competitiveness and the European FEDER funds: MORPHSED (CGL2012-36394) and MORPHPEAK (CGL2016-78874-R). The first author has a grant funded by the Ministry of Education, Culture and Sports, Spain (FPU016/01687). The last author is a Serra Húnter Fellow at the University of Lleida. The first and last authors are part of the Fluvial Dynamics Research Group-RIUS, a Consolidated Group recognized by the Generalitat de Catalunya (2017 SGR 459645). We also acknowledge the support of the CERCA Program of the Generalitat de Catalunya. Finally, we also thank the British Society for Geomorphology to support the long-term geomorphological monitoring program in the experimental badland that started in 2013; and the members of the Fluvial Dynamics Research Group for their assistance during the fieldwork campaigns. We thank Prof. Stuart Lane, acting as editor in chief of the journal *Earth Surface Processes and Landforms*, his suggestion of considering the methodological paper submitted by Llena et al. (2020) where the MaGPiE algorithm is presented and this one as a paper pair or two connected papers. Finally, we thank all comments and suggestions received from two anonymous referees, and from the associate editor and the editor in chief of *Earth Surface Processes and Landforms*. All their comments have helped to clarify and improve this paper.

Data availability statement

Research data not shared

Conflict of interest statement

The authors have no conflicts of interest to declare

References

- Anderson SW. 2019. Uncertainty in quantitative analyses of topographic change: error propagation and the role of thresholding. *Earth Surface Processes and Landforms* 44: 1015-1033.
- Aucelli PPC, Conforti M, Della Seta M, Del Monte M, D'uva L, Roskopf CM, Vergari F. 2016. Multi-temporal Digital Photogrammetric Analysis for Quantitative Assessment of Soil Erosion Rates in the Landola Catchment of the Upper Orcia Valley (Tuscany, Italy). *Land Degradation and Development* 27: 1075– 1092
- Balasch JC, Clotet N, Gallart F. 1988. Validación a escala temporal de tasas de erosión en áreas de badlands (Prepirineo Catalán). *Comunicaciones Congreso Geológico de España* 1: 359-362.
- Ballesteros-Cánovas JA, Stoffel M, Martín-Duque JF, Corona C, Lucía A, Bodoque JM, Montgomery DR. 2017. Gully evolution and geomorphic adjustments of badlands to reforestation. *Scientific Reports*. 8 pp.
- Bangen SG, Kramer N, Wheaton, JM, and Bouwes N. 2017. The GUTs of the Geomorphic Unit Tool: What is under the hood. EP31D-1901. AGU. New Orleans, LA, 11-15 Dec.
- Barnes N, Luffman I, Nandi A. 2016. Gully erosion and freeze-thaw processes in clay-rich soils, northeast Tennessee, USA. *GeoResJ* 1-12: 67-76
- Benito G, Gutiérrez M, Sancho C. 1992. Erosion Rates in Badland Areas of the Central Ebro Basin (NE-Spain). *Catena* 19: 269-286.
- Bishop A and Morgenstern N. 1960. Stability coefficients for earth slopes. *Geotechnique* 10: 129–150.
- Borselli L, Cassi P, Torri D. 2008. Prolegomena to sediment and flow connectivity in the landscape: A GIS and field numerical assessment. *Catena* 75: 268–277.
- Brasington J, Rumsby B, McVey R, 2000. Monitoring and Modelling Morphological Change in a Braided Gravel-Bed River Using High Resolution GPS-Based Survey. *Earth Surface Processes and Landforms* 25: 973-990.
- Brasington J, Vericat D, Rychkov I. 2012. Modelling river bed morphology, roughness, and surface sedimentology using high resolution terrestrial laser scanning. *Water Resources Research*. 48: 1-18.
- Bryan R, Yair A. 1982. Perspectives on studies of badland geomorphology. In: *Badland Geomorphology and Piping*, Bryan RB, Yair A (Eds.). Geobooks: Norwich; 1–12.

- Calvo-Cases A, Harvey AM. 1996. Morphology and development of selected badlands in Southeast Spain: Implications of climatic change. *Earth Surface Processes and Landforms* 21: 725-735.
- Canton Y, Domingo F, Solé-Benet, Puigdefàbregas J. 2000. Hydrological and erosion response of a badlands system in semiarid SE Spain. *Journal of Hydrology* 252: 65-84.
- Cavalli M, Trevisani S, Comiti F, Marchi L, 2013. Geomorphometric assessment of spatial sediment connectivity in small Alpine catchments. *Geomorphology* 188: 31-41.
- Cerdà A. 1997. Influencia de la Litología en los procesos de erosión en badlands. Los casos de Anna (Valencia) y Petrer (Alicante). *Pirineos* 149: 3-20.
- Clotet N, Gallart F, Sala M. 1987. Los badlands: características, interés teórico, dinámica y tasas de erosión. *Notes de Geografía Física* 15-16: 28-37.
- Clotet-Perarnau N, Gallart F, Balasch JC.. 1988. Medium-term erosion rates in small scarcely vegetated catchment in the Pyrenees. *Catena Supplement* 13: 37-47.
- De Ploey J, Gabriels D. 1980. Measuring soil loss and experimental studies. In: M.J. Kirkby and R.P.C. Morgan (Editors). *Soil Erosion*. Willey, 63-108 pp.
- Descroix L, Olivry JC. 2002. Spatial and temporal factors of erosion by water of black marls in the badlands of the French southern Alps. *Hydrological Sciences Journal* 47(2): 227-242.
- Desir G, Marín C. 2013. Role of erosion processes on the morphogenesis of a semiarid badland area. Bardenas Reales (NE Spain). *Catena* 106: 83-92.
- Faulkner H. 2008. Connectivity as a crucial determinant of badland morphology and evolution. *Geomorphology*. 100: 91-103.
- Faulkner H. 2018. The Role of Piping in the Development of Badlands. In: *Badland Dynamics in the Context of Global Change*. Nadal-Romero E, Martínez-Murillo JF, Kuhn NJ. (Eds.). Elsevier, Amsterdam. 217-253.
- Ferrer V, Errea P, Alonso E, Gómez-Guitierrez A, Nadal-Romero E. 2017. A Multiscale Approach to asses Geomorphological Processes in a semiarid badland area (Ebro Depression, Spain). *Cuadernos de Investigación geográfica* 43: 41-62.
- Francke T, López-Tarazón JA, Vericat D, Bronstert A, Batalla RJ. 2008. Flood-based analysis of high-magnitude sediment transport using a non-parametric method. *Earth Surface Processes and Landforms* 33: 2064-2077.
- Gallart F, Solé A, Puigdefàbregas J, Lázaro R. 2002. Badland Systems in the Mediterranean. In: *Dryland Rivers: Hydrology and Geomorphology of Semi-arid Channels*. Bull LJ, Kirkby MJ (Eds.). John Wiley & Sons, Ltd. 299-326.
- Gallart F, Marignani M, Pérez-Gallego N, Santi E, Maccherini S. 2013. Thirty years of studies on badlands, from physical to vegetational approaches. A succinct review. *Catena* 106: 4-11.
- Girardeau-Montaut D. 2019. CloudCompare - Open Source Project. <http://www.danielgm.net/cc/> (accessed 01 February 2019).
- Greenwalt CR, Schultz ME. 1968. Principles of Error Theory and Cartographic Applications, US Air Force Aeronautical Chart and Information Center Technical Report No. 96. US Air Force Aeronautical Chart and Information Center: St Louis, MO; 98 pp.

Grenfell SE, Rowntree KM, Grenfell MC. 2012. Morphodynamics of a gully and floodout system in the Sneeu Berg Mountains of the semi-arid Karoo, South Africa: Implications for local landscape connectivity. *Catena* 89: 8-21.

Gutiérrez M, Sancho C, Benito G, Sirvent J, Desir G. 1997 Quantitative study of piping processes in badland áreas of the Ebro Basin, NE Spain. *Geomorphology* 20: 237-253.

Kasanin-Grubin M. 2013. Clay mineralogy as a crucial factor in badlands hillslope processes. *Catena* 106: 54–67.

Krenz J, Kuhn NJ. 2018. Assessing Badland Sediment Sources Using Unmanned Aerial Vehicles. In: *Badland Dynamics in the Context of Global Change*. Nadal-Romero E, Martínez-Murillo JF, Kuhn NJ. (Eds.). Elsevier, Amsterdam. 320 pp.

Lague D, Brodu N, Leroux J. 2013. Accurate 3D comparison of complex topography with terrestrial laser scanner: Application to the Rangitikei canyon (N-Z). *ISPRS Journal of Photogrammetry and Remote Sensing* 82: 10-26.

Lane SN, Westaway RM, Hicks DM. 2003. Estimation of Erosion and Deposition Volumes in a Large, Gravel-Bed, Braided River Using Synoptic Remote Sensing. *Earth Surface Processes and Landforms* 28: 249-271.

Llena M, Smith MW, Vericat D. 2018. The role of the altitude and surface morphometric proprieties in the quality of SfM-based High Resolution Topography. In *Geomorfología del Antropoceno. Efectos del Cambio Global sobre los procesos geomorfológicos*. Garcia C, Gómez--Pujol L, Morán-Tejeda E, Batalla RJ (eds). Universitat de les Illes Balears - Sociedad Española de Geomorfología: Palma. 402 pp.

Llena M, Vericat D, Smith MW, Wheaton JM. 2020. Geomorphic process signatures reshaping sub-humid Mediterranean badlands: 1. Methodological development based on High Resolution Topography. *Earth Surface Processes and Landforms*. This Issue.

Lucia A, Martín-Duque JF, Laronne JB, Sanz-Santos MA. 2011. Geomorphic dynamics of gullies developed in sandy slopes of Central Spain. *Landform Analysis* 17: 91-97.

Marchamalo M, Hooke JM, Sandercock PJ. 2016. Flow and sediment connectivity in semi-arid landscapes in SE Spain: patterns and controls. *Land Degradation and Development* 27: 1034-1044.

Martínez-Casasnovas JA, Poch RM. 1998. Estado de la Conservación de los suelos de la cuenca del embalse Joaquín Costa. *Limnimética* 14: 83-91.

Mathys N, Brochot S, Meunier M, Richard D. 2003. Erosion quantification in the small marly experimental catchments of Draix (Alpes de Haute Provence, France). Calibration of the ETC rainfall–runoff–erosion model. *Catena* 50: 527-548.

Milan DJ, Heritage GL, Large ARG, Fuller IC. 2011. Filtering spatial error from DEMs: implications for morphological change estimation. *Geomorphology* 125: 160–171.

Moreno-de las Heras M, Gallart F. 2016. Lithology controls the regional distribution and morphological diversity of montane Mediterranean badlands in the upper Llobregat basin (eastern Pyrenees). *Geomorphology* 273: 107-115.

Moreno-de las Heras M, Gallart F. 2018. The Origin of Badlands. In: *Badland Dynamics in the Context of Global Change*. Nadal-Romero E, Martínez-Murillo JF, Kuhn NJ. (Eds.). Elsevier, Amsterdam. 320 pp.

Morgenstern N, Price VE. 1965. The analysis of the stability of general slip surfaces. *Geotechnique* 15(1): 79–93.

Mosbrucker AR, Major JJ, Spicer KR, Pitlick J. 2017. Camera system considerations for geomorphic applications of SfM photogrammetry. *Earth Surface Processes and Landforms*. 42: 969-986.

Nadal-Romero E, Regüés D, Martí-Bono C, Serrano-Muela P. 2007. Badland dynamics in the Central Pyrenees: temporal and spatial patterns of weathering processes. *Earth Surface Processes and Landforms* 32: 888-904.

Nadal-Romero E, Regüés D. 2010. Geomorphological dynamics of sub-humid mountain badland areas: weathering, hydrological and suspended sediment transport processes. A case of study in the Araguás catchment (Central Pyrenees), and implications for altered hydro-climatic regimes. *Progress in Physical Geography* 34 (3): 123–150.

Nadal-Romero E, Petric K, Verachtert, Bochet E, Poesen J. 2014. Effects of slope angle and aspect on plant cover and species richness in a humid Mediterranean badland. *Earth Surface Processes and Landforms* 39: 1705-1716.

Nadal-Romero E, Revuelto J, Errea P, López-Moreno JI. 2015. The application of terrestrial laser scanner and SfM photogrammetry in measuring erosion and deposition processes in two opposite slopes in a humid badlands area (central Spanish Pyrenees). *SOIL* 1, 561–573.

Nadal-Romero E, García-Ruiz JM. 2018. Rethinking Spatial and Temporal Variability of Erosion in Badlands. In: *Badland Dynamics in the Context of Global Change*. Nadal-Romero E, Martínez-Murillo JF, Kuhn NJ. (Eds.). Elsevier, Amsterdam. 320 pp.

Nobajas A, Waller RI, Robinson ZP, Sangonzalo R. 2017. Too much of a good thing? the role of detailed UAV imagery in characterizing large-scale badland drainage characteristics in South-Eastern Spain. *International Journal of Remote Sensing* 38: 2845-2860.

Passalacqua P, Belmont P, Staley DM, Simley JD, Arrowsmith JR, Bode CA, Crosby C, DeLong SB, Glenn NF, Kelly SA, Lague D, Sangireddy H, Schaffrath K, Tarboton DG, Wasklewicz T, Wheaton JM. 2015. Analyzing high resolution topography for advancing the understanding of mass and energy transfer through landscapes: a review. *Earth-Science Reviews* 148: 174-193.

Pennock DJ, Zebarth BJ, De Jong E, 1987. Landform classification and soil distribution in hummocky terrain, Saskatchewan, Canada. *Geoderma* 40 (3–4): 297–315.

Pimentel D, Harvey C, Resosudamo P, Sinclair K, Kurz D, McNair M, Crist S, Shpritz L, Fitton L, Saffouri R, Blair R. 1995. Environmental and Economic Costs of Soil Erosion and Conservation Benefits. *Science* 267: 1117-1122.

Piqué G, López-Tarazón JA, Batalla RJ. 2014. Variability of in-channel sediment storage in a river draining highly erodible areas (the Isábena, Ebro basin). *J Soils Sediments* 12: 2031-2044.

Rainato R, Mao L, García-Rama A, Picco L, Cesca M, Vianello A, Preciso E, Scussel GR, Lenzi MA. 2017. Three decades of monitoring in the Rio Cordon instrumented basin: Sediment budget and temporal trend of sediment yield. *Geomorphology* 291: 45-56.

Regüés D, Pardini G, Gallart F. 1995. Regolith behavior and physical weathering of clayey mudrock as dependent on seasonal weather conditions in a badland area at Vallcebre, Eastern Pyrenees. *Catena* 25: 199-212.

Regüés D, Guàrdia R, Gallart F. 2000. Geomorphic agents versus vegetation spreading as causes of badland occurrence in a Mediterranean subhumid mountainous area. *Catena* 40(2): 173–187.

Richard D, Mathys N. 1999. Historique, contexte technique et scientifique des BVRE de Draix. In: N. Mathys (Ed.), *Caractéristiques, données disponibles et principaux résultats acquis au cours des dix ans de suivi*. Actes du séminaire Les bassins versants expérimentaux de Draix. Cemagref-Editions, Coll. Actes de colloques, Grenoble, 11-28 pp.

Rossi RK. 2018. *Evaluation of 'Structure-from-Motion' from a Pole-Mounted Camera for Monitoring Geomorphic Change*. Master Dissertation. Utah State University. 211 pp.

Rychkov, I., Brasington, J., Vericat D. 2012. Computational and methodological aspects of terrestrial surface analysis based on point clouds. *Computers & Geosciences*. 42: 64-70.

Sirvent J, Desir G, Gutierrez M, Sancho C, Benito G. 1997. Erosion rates in badland areas recorded by collectors, erosion pins and profi lometer techniques (Ebro Basin, NE-Spain). *Geomorphology* 18: 61–75.

Smith KG. 1958. Erosional processes and landforms in Badlands National Monument, South Dakota. *Bulletin of the Geological Society of America* 69: 975-1008.

Smith MW, Vericat D. 2015. From experimental plots to experimental landscapes: topography, erosion and deposition in sub-humid badlands from Structure-from-motion photogrammetry. *Earth Surface Processes and Landforms* 40: 1656-1671.

Smith MW, Carrivick JL, Quincey DJ. 2016. Structure from motion photogrammetry in physical geography. *Progress in Physical Geography* 40(2): 247-275.

Solé-Benet A, Afana A, Cantón Y. 2012. Erosion pins, profile and laser scanners for soil erosion monitoring in active hillslopes in badlands of SE Spain. *Actas XII Reunión Nacional de Geomorfología, Santander* 575-578.

Stöcker C, Eltner A, Karrasch P. 2015. Measuring gullies by synergetic application of UAV and close range photogrammetry — a case study from Andalusia, Spain. *Catena* 132: 1–11.

Tarolli, P. 2014. High-resolution topography for understanding Earth surface processes: opportunities and challenges. *Geomorphology* 216: 295–312.

Torri D, Colica A, Rockwell D. 1994. Preliminary study of the erosion mechanisms in a biancana badland (Tuscany, Italy). *Catena* 23: 281-294.

Torri D, Rossi M, Brogi F, Marignani M, Bacaro G, Santi E, Tordoni E, Amici V, Maccherini S. 2018. Badlands and the Dynamics of Human History, Land Use, and Vegetation Through Centuries. In: *Badland Dynamics in the Context of Global Change*. Nadal-Romero E, Martínez-Murillo JF, Kuhn NJ. (Eds.). Elsevier, Amsterdam. 320 pp.

Tsutsumi D, Fujita M. 2016. Field observations, experiments, and modeling of sediment production from freeze and thaw action on a bare, weathered granite slope in a temperate region of Japan. *Geomorphology* 267: 37-47.

Vericat D, Smith MW, Brasington J. 2014. Patterns of topographic change in sub-humid badlands determined by high resolution multi-temporal topographic surveys. *Catena* 120: 164–176.

Vericat D, Wheaton J, Brasington J. 2017. Revisiting the Morphological Approach: Opportunities and Challenges with Repeat High-Resolution Topography. In: Gravel-Bed Rivers: Processes and Disasters. Tsutsumi DT, Laronne JB. (Eds.). Wiley, 121-158.

Westaway RM, Lane SN, Hicks DM. 2003. Remote survey of large- scale braided, gravel-bed rivers using digital photogrammetry and image analysis. *International Journal of Remote Sensing* 24(4): 795–815.

Williams RD, Brasington J, Vericat D, Hicks DM. 2014. Hyperscale terrain modelling of braided rivers: fusing mobile terrestrial laser scanning and optical bathymetric mapping. *Earth Surface Processes and Landforms* 39: 167-183.

Wheaton JM, Brasington J, Darby SE, Sear DA. 2010. Accounting for uncertainty in DEMs from repeat topographic surveys: improved sediment budgets. *Earth Surface Processes and Landforms* 35(2): 136–156.

Wheaton JM, Fryirs K, Brierly G, Bangen SG, Bouwes N, and O'Brien G. 2015. Geomorphic mapping and taxonomy of fluvial landforms. *Geomorphology* 248: 273–295.

Yair A, Lavee H, Bryan RB, Adar E. 1980. Runoff and erosion processes and rates in the Zin Valley badlands, Northern Negev, Israel. *Earth Surface Processes* 5: 205-225.

Table 1. Main characteristics of the two experimental badlands.

| | Badland 1 (B1) | Badland 2 (B2) |
|--|-------------------|-------------------|
| Surface (ha) | 0.32 | 0.12 |
| Mean Altitude (m a.s.l) | 590.74 | 601.70 |
| Vegetation cover (%) | 17.70 | 10.88 |
| Mean aspect (°) | 210.67 (SW) | 174.08 (S) |
| Mean Slope (°) | 31.44 | 37.27 |
| Mean slope of dip strata (°) | 25 | 40 |
| Mean slope of shady aspect (°) | 34.25 | 48.84 |
| Mean Roughness (mm)* | 7.52 | 6.96 |
| Mean Topographic Wetness Index** | 0.41 | 0.16 |
| Normalized mean value of Index of Sediment Connectivity*** | -2.84 | -1.02 |

* Detrended standard deviation of observation elevations per each 0.05 x 0.05 m grid.

** Calculated by means of the expression $\ln(A/\tan\beta)$ where A is referred to the upslope area in a given cell, and β is the local slope.

*** Calculated by the approach of Cavalli et al. (2013) from the ratio between upslope component (i.e. contributing area, roughness and slope) and downslope component (i.e. flow path length, roughness and slope). Index value is normalized by the micro-catchment surface.

Table 2. Description of the meteorological variables analysed, unites and associated abbreviations.

| Type of variable | Abbreviation | Description | Unit |
|------------------|--------------|---|-----------------------|
| Time | ND | Number of days in between surveyed periods | Day |
| Rainfall | TR | Total rainfall | mm |
| | RD | Rainfall duration | Hour |
| | MRI | Mean rainfall intensity | mm hour ⁻¹ |
| | MaxRI | Maximum rainfall intensity | mm hour ⁻¹ |
| | MT | Mean temperature | °C |
| Temperature | Zd | Days with temperatures <0°C | Day |
| | MTZD | Mean temperature of the minimum temperatures of days <0°C | °C |
| | MinTZD | Minimum temperature | °C |

Table 3. Summary of the topographic surveys and quality assessment for both badlands. Note that the Georeferencing Errors (GE) of the Structure from Motion (SfM) based surveys were calculated from the Root Mean Square Error (RMSE) of the Ground Control Points (GCPs). In the case of the Terrestrial Laser Scanner (TLS) surveys, the GE includes the error associated to the registration of the different stations and the georeferencing of the point clouds. Mean Absolute Error (MAE) and Standard Deviation Error (SDE) were calculated based on the check points (ChPs). The accuracy of the MaGPIE classification results is also presented by the Classification Agreement (CA).

| Survey | Date | Badlands surveyed | Method | BADLAND 1 | | | | | | BADLAND 2 | | | | | |
|--------|------------|-------------------|--------|-------------|---------|-----------|----------|----------|--------|-------------|---------|-----------|----------|----------|--------|
| | | | | Photos (n°) | GE (cm) | ChPs (n°) | MAE (cm) | SDE (cm) | CA (%) | Photos (n°) | GE (cm) | ChPs (n°) | MAE (cm) | SDE (cm) | CA (%) |
| S01 | 26/06/2013 | 1 | TLS | - | 0.31 | - | - | - | 81 | - | - | - | - | - | - |
| S02 | 29/05/2014 | 1 | TLS | - | 0.27 | 568 | 1.16 | 1.66 | 67 | - | - | - | - | - | - |
| S03 | 04/08/2015 | 1 | SfM | 237 | 2.25 | 260 | 1.60 | 2.09 | 77 | - | - | - | - | - | - |
| S04 | 19/07/2016 | 1 | SfM | 475 | 1.87 | 270 | 1.87 | 2.61 | 81 | - | - | - | - | - | - |
| S05 | 07/12/2016 | 1 and 2 | SfM | 740 | 2.19 | 256 | 1.57 | 2.14 | 82 | 320 | 3.52 | 95 | 2.49 | 3.27 | 68 |
| S06 | 04/04/2017 | 1 and 2 | SfM | 525 | 1.91 | 238 | 1.25 | 1.67 | 84 | 332 | 4.11 | 244 | 3.48 | 3.98 | 65 |
| S07 | 28/06/2017 | 1 and 2 | SfM | 889 | 2.22 | 413 | 1.72 | 2.29 | 62 | 326 | 2.64 | 357 | 1.82 | 2.29 | 64 |
| S08 | 08/11/2017 | 1 and 2 | SfM | 497 | 2.14 | 518 | 2.25 | 2.81 | 82 | 305 | 1.78 | 572 | 2.21 | 2.29 | 85 |
| S09 | 23/03/2018 | 1 and 2 | SfM | 579 | 1.80 | 271 | 2.36 | 2.82 | 81 | 372 | 1.79 | 116 | 1.71 | 2.21 | 83 |
| S10 | 18/06/2018 | 1 and 2 | SfM | 446 | 2.23 | 259 | 1.60 | 2.09 | 72 | 225 | 1.46 | 128 | 1.79 | 2.43 | 73 |

Table 4. Summary of the meteorological variables during the study period grouped on annual and seasonal scales (see table 3 for the meaning of the abbreviations).

| | Code | Period | Survey period | ND (days) | TR (mm) | RD (hours) | MRI (mm/hour) | MaxRI (mm/hour) | MT (°C) | Zd (days) | MTZD (°C) | MinTZD (°C) |
|----------------|-------|-------------|---------------|-----------|---------|------------|---------------|-----------------|---------|-----------|-----------|-------------|
| Annual Scale | 13-14 | 2013-2014 | S01 – S02 | 338 | 794 | 299.00 | 2.65 | 20.40 | 12.60 | 50 | -1.44 | -6.20 |
| | 14-15 | 2014-2015 | S02 – S03 | 433 | 819 | 321.75 | 2.54 | 25.60 | 14.80 | 49 | -1.79 | -6.00 |
| | 15-16 | 2015-2016 | S03 – S04 | 351 | 657 | 168.08 | 3.91 | 21.60 | 13.10 | 31 | -1.29 | -3.90 |
| | 16-17 | 2016-2017 | S04 – S07 | 345 | 818 | 519.67 | 1.57 | 24.60 | 13.40 | 86 | -1.90 | -9.89 |
| | 17-18 | 2017-2018 | S07 – S10 | 356 | 1001 | 550.08 | 1.82 | 17.40 | 11.80 | 109 | -2.25 | -7.66 |
| Seasonal Scale | A2016 | Autumn 2016 | S04 – S05 | 142 | 355 | 163.42 | 2.17 | 20.40 | 18.20 | 13 | -1.35 | -4.19 |
| | W2016 | Winter 2016 | S05 – S06 | 119 | 254 | 171.25 | 1.49 | 10.20 | 5.10 | 70 | -3.28 | -9.89 |
| | S2017 | Spring 2017 | S06 – S07 | 86 | 209 | 185.00 | 1.13 | 24.60 | 17.10 | 3 | -1.06 | -2.16 |
| | A2017 | Autumn 2017 | S07 – S08 | 134 | 246 | 117.50 | 2.09 | 17.40 | 19.00 | 0 | - | - |
| | W2017 | Winter 2017 | S08 – S09 | 136 | 362 | 158.42 | 2.29 | 7.99 | 3.80 | 102 | -2.94 | -7.66 |
| | S2018 | Spring 2018 | S09 – S10 | 88 | 393 | 232.58 | 1.69 | 16.59 | 13.30 | 7 | -1.56 | -3.54 |

*Note that ND > 365 indicates the second survey was performed slightly ahead of one year after the first.

Table 5. Summary of observed topographic changes extracted from thresholded DoDs for the different temporal scales analysed in the paper.

| Study period | BADLAND 1 | | | | | | | BADLAND 2 | | | | | | |
|----------------|---------------------------------|---------|-------------------------------------|---------|------------|---------------------------------------|--|---------------------------------|---------|-------------------------------------|---------|------------|---------------------------------------|--|
| | Areal changes (m ²) | | Volume Difference (m ³) | | | Average Net Thickness Difference (cm) | Area with changes above the minLoD (% total) | Areal changes (m ²) | | Volume Difference (m ³) | | | Average Net Thickness Difference (cm) | Area with changes above the minLoD (% total) |
| | Lowering | Raising | Lowering | Raising | Net change | | | Lowering | Raising | Lowering | Raising | Net change | | |
| Annual Scale | 13-14 | 39.11 | 3.57 | 4.17 | 0.3 | -3.86 | -0.15 | 1.66 | - | - | - | - | - | - |
| | 14-15 | 14.24 | 17.92 | 1.22 | 1.37 | 0.15 | 0.01 | 1.22 | - | - | - | - | - | - |
| | 15-16 | 21.75 | 5.42 | 1.78 | 0.69 | -1.09 | -0.05 | 1.14 | - | - | - | - | - | - |
| | 16-17 | 65.65 | 11.22 | 5.3 | 1.96 | -3.34 | -0.13 | 3.10 | 28.22 | 11.62 | 2.1 | 1.47 | -0.63 | -0.06 |
| | 17-18 | 41.78 | 34.69 | 3.83 | 3.08 | -0.75 | -0.03 | 3.11 | 25.6 | 25.76 | 2.58 | 2.94 | 0.36 | 0.04 |
| Seasonal Scale | A2016 | 44.79 | 9.21 | 3.42 | 1.71 | -1.7 | -0.07 | 2.08 | - | - | - | - | - | - |
| | W2016 | 14.69 | 28.07 | 1.52 | 2.28 | 0.77 | 0.03 | 1.59 | 24.42 | 19.18 | 2.51 | 2.09 | -0.42 | -0.04 |
| | S2017 | 43.13 | 34.58 | 3.42 | 3.09 | -0.33 | -0.01 | 3.11 | 26.69 | 14.58 | 2.14 | 1.69 | -0.45 | -0.04 |
| | A2017 | 15.08 | 31.09 | 1.23 | 2.63 | 1.4 | 0.06 | 1.83 | 18.96 | 8.37 | 1.84 | 0.66 | -1.18 | -0.11 |
| | W2017 | 32.52 | 35.9 | 2.92 | 3.14 | 0.23 | 0.01 | 2.47 | 13.58 | 22.67 | 1.54 | 2.48 | 0.94 | 0.09 |
| Totals | S2018 | 45.54 | 21.5 | 4.29 | 1.88 | -2.41 | -0.09 | 2.59 | 15.61 | 19.17 | 1.51 | 2.01 | 0.5 | 0.05 |
| | 16-18 | 84.62 | 20.67 | 7.2 | 2.89 | -4.31 | -0.86 | 4.19 | 69.64 | 27.31 | 5.74 | 3.48 | -2.26 | -0.22 |
| | 13-18 | 247.97 | 9.93 | 21.95 | 1.03 | -20.92 | -4.09 | 10.54 | - | - | - | - | - | - |

Table 6. Pearson correlation results between meteorological variables and topographic changes segregated by the main geomorphic processes in Badland 1 (B1) and Badland 2 (B2). Highlighted values represent significant correlations at $p < 0.05$. Note that the abbreviations of the variables are presented in table 2.

| | | Change | ND | TR | RD | MRI | MaxRI | MT | Zd | MTZD | MinTZD |
|----|------------------------|--------|--------------|-------------|-------------|--------------|-------|--------------|-------------|-------------|-------------|
| B1 | Mass Wasting | - | 0.02 | 0.23 | 0.46 | 0.33 | 0.15 | 0.33 | 0.55 | 0.42 | 0.55 |
| | | + | -0.64 | -0.48 | -0.04 | -0.73 | -0.40 | -0.11 | 0.12 | -0.18 | 0.01 |
| | Rilling and Gullying | - | 0.11 | 0.25 | 0.43 | 0.29 | 0.18 | 0.14 | 0.23 | 0.14 | 0.09 |
| | | + | 0.02 | 0.00 | 0.28 | -0.53 | 0.17 | 0.03 | 0.24 | -0.12 | -0.10 |
| | Cutting and Filling | - | -0.10 | 0.33 | 0.54 | 0.28 | -0.35 | -0.21 | 0.08 | -0.15 | 0.15 |
| | | + | -0.22 | -0.12 | 0.15 | -0.42 | -0.40 | -0.28 | 0.46 | -0.27 | -0.13 |
| | Sheet Washing | - | -0.08 | 0.19 | 0.44 | 0.31 | -0.34 | -0.10 | 0.21 | 0.11 | 0.39 |
| | Regolith Cohesion Loss | + | -0.44 | -0.32 | -0.05 | -0.48 | -0.44 | -0.13 | 0.10 | -0.02 | 0.21 |
| | Overlapping Processes | - / + | 0.35 | -0.15 | -0.48 | 0.36 | 0.31 | 0.32 | 0.41 | 0.10 | -0.06 |
| | TOTAL CHANGE | | 0.25 | 0.05 | 0.48 | 0.65 | 0.08 | 0.07 | 0.35 | 0.18 | 0.25 |
| B2 | Mass Wasting | - | 0.40 | 0.26 | 0.28 | -0.18 | -0.23 | -0.52 | 0.65 | 0.64 | 0.73 |
| | | + | 0.12 | 0.31 | 0.32 | -0.35 | -0.21 | -0.49 | 0.42 | -0.19 | -0.48 |
| | Rilling and Gullying | - | 0.93 | 0.81 | 0.82 | -0.04 | 0.45 | 0.18 | 0.54 | -0.01 | 0.38 |
| | | + | 0.18 | 0.28 | 0.11 | 0.60 | -0.61 | -0.64 | 0.68 | -0.55 | -0.33 |
| | Cutting and Filling | - | -0.05 | 0.10 | 0.16 | -0.37 | 0.58 | -0.77 | -0.62 | -0.65 | -0.63 |
| | | + | 0.38 | 0.50 | 0.35 | 0.52 | -0.54 | -0.72 | 0.83 | -0.55 | -0.57 |
| | Sheet Washing | - | -0.10 | -0.14 | -0.06 | -0.59 | -0.05 | -0.11 | -0.01 | 0.25 | 0.15 |
| | Regolith Cohesion Loss | + | 0.61 | 0.65 | 0.42 | -0.20 | 0.66 | 0.62 | -0.07 | 0.73 | 0.13 |
| | Overlapping Processes | - / + | -0.43 | -0.07 | -0.16 | 0.44 | 0.14 | -0.2 | 0.22 | 0.39 | 0.24 |
| | TOTAL CHANGE | | 0.43 | 0.53 | 0.51 | 0.16 | 0.24 | 0.54 | 0.70 | 0.71 | 0.63 |

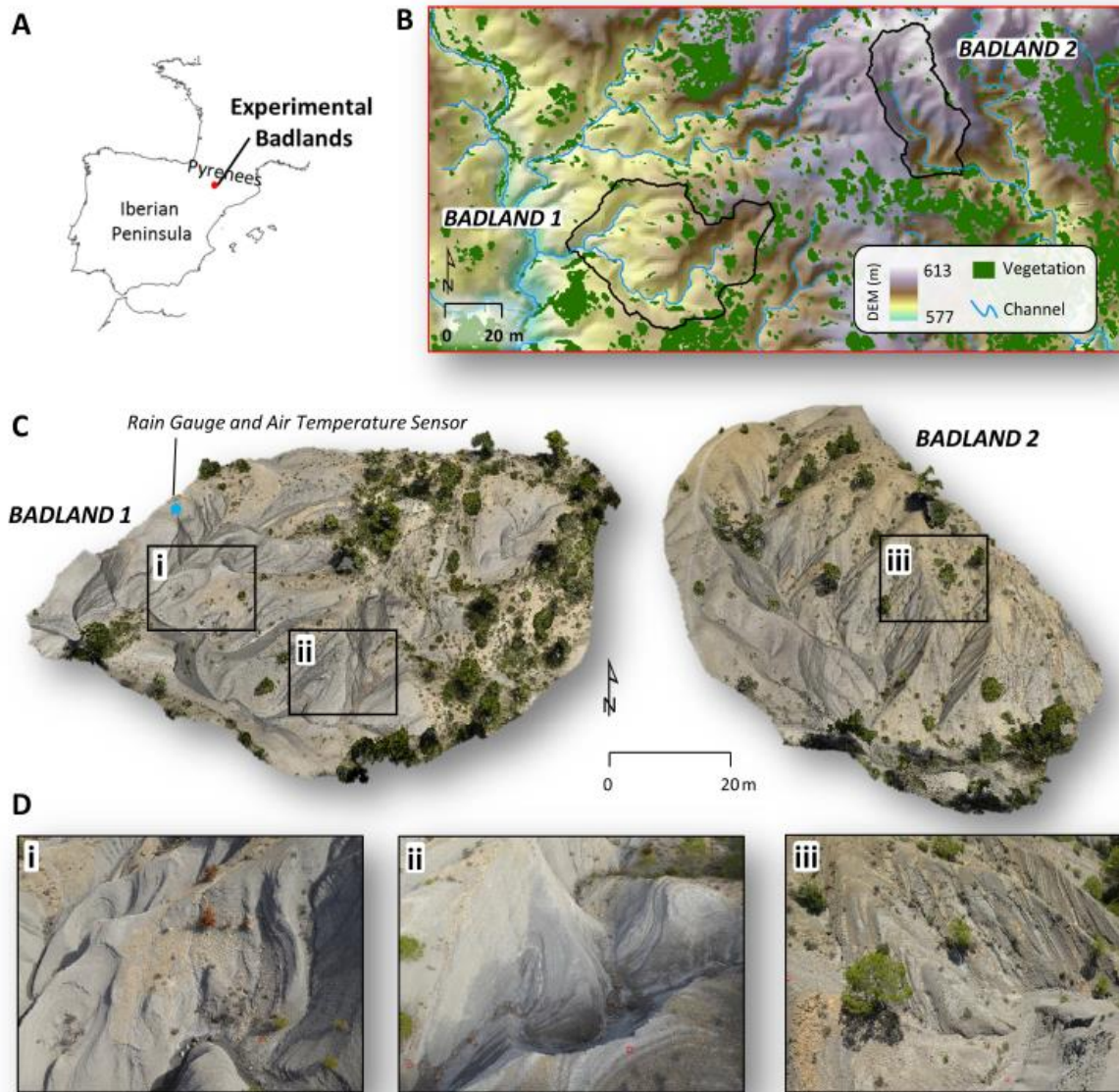


Figure 1. (A) Location of the experimental badlands in the Iberian Peninsula (red dot) and photo-rendered point clouds of the two badlands (i.e. Badland 1 –B1- and Badland 2 –B2- respectively). The blue dot in B1 indicates the location of both the Rain Gauge and the Temperature Sensors. (B) Close photo views of the experimental badlands.

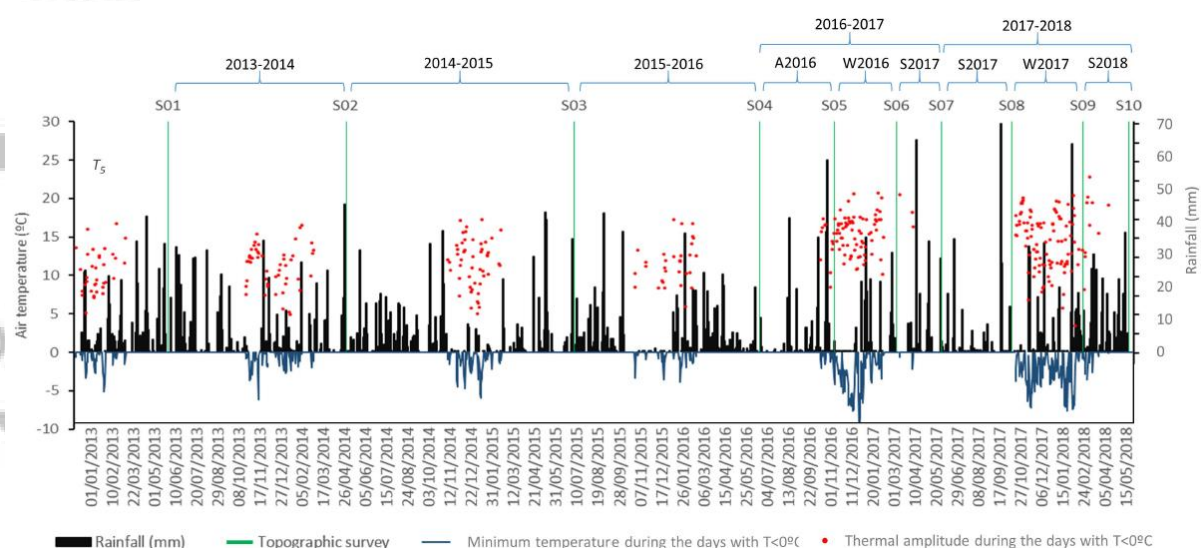


Figure 2. Meteorological data registered during all the study period indicating the different topographic surveys (green columns) and analysed periods (blue brackets). Black columns represent total daily rainfall, blue line represents the minimum temperature registered during the days with temperatures below 0°C , and red dots indicates the thermal amplitude for the days in which temperatures below 0°C were registered.

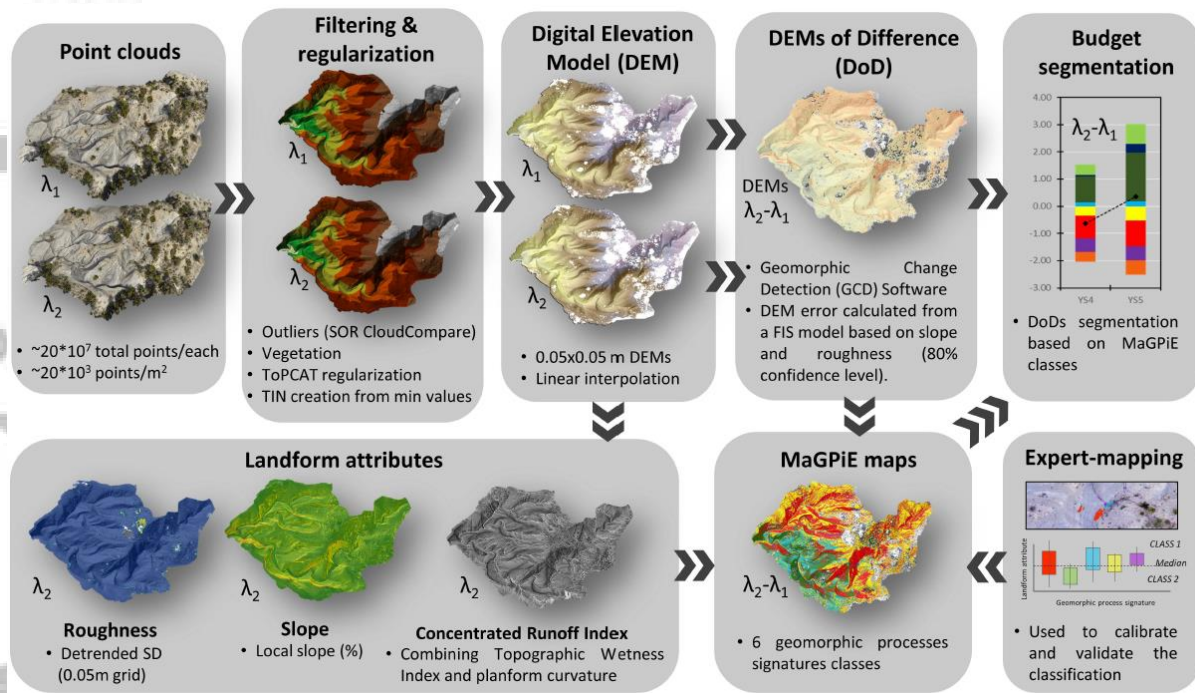


Figure 3. General workflow to obtain the geomorphic processes maps from the starting point clouds through several intermediate steps (i.e. filtering, DEMs obtaining, DoDs calculation, MaGPiE parametrization). See more details in Llena et al. (2020).

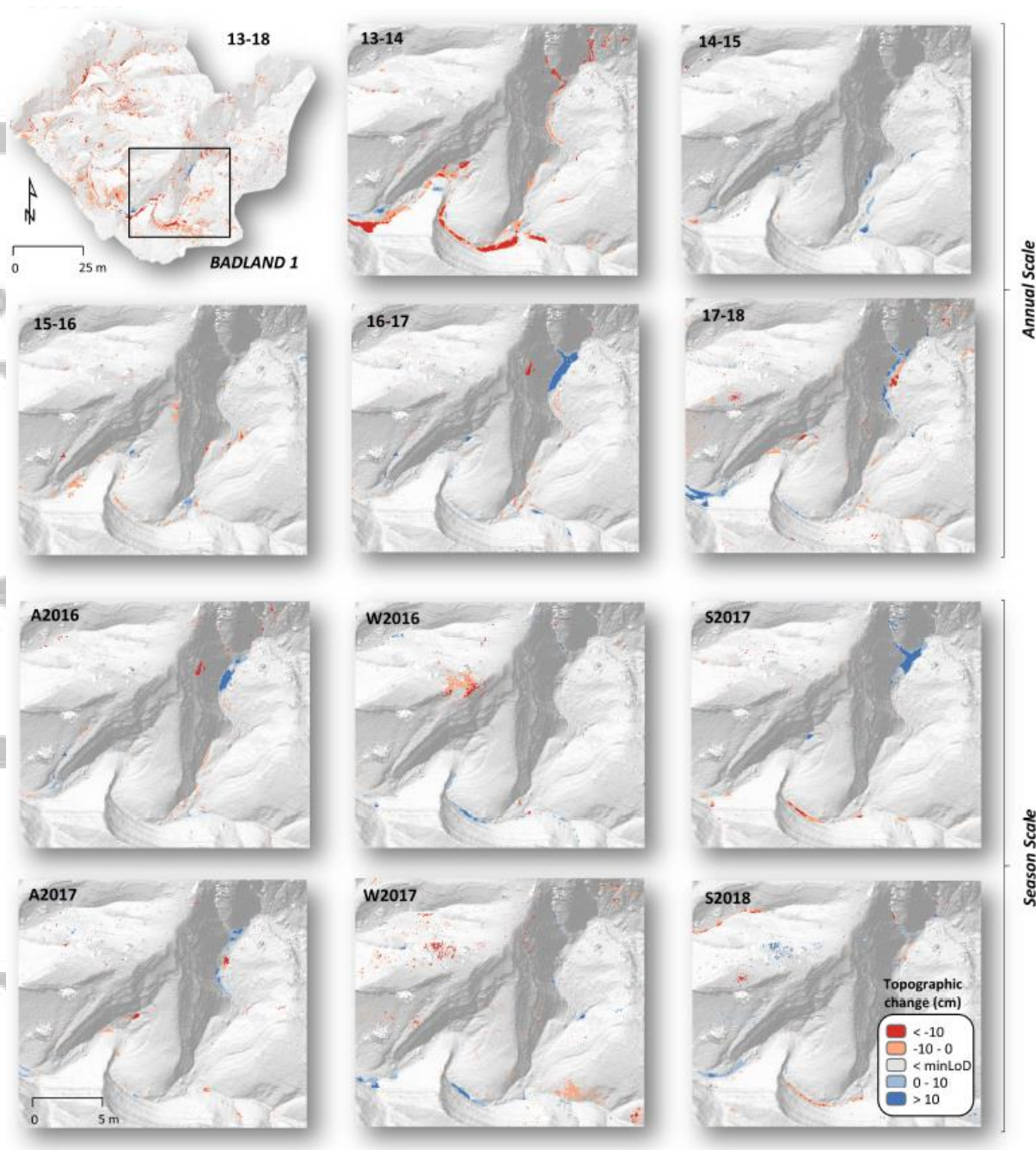


Figure 4. DoD maps of a representative area of B1 for the different analysed temporal scales: annual (upper part) and seasonal (lower part) scales. Note that the DoD of the entire badland (top left) corresponds to the map associated with the complete study period (2013-2018) in this badland. The location of the representative area is also shown. Changes below the minimum level of detection (i.e. minLoD) are not presented (considered uncertain) and an underlying shaded DEM is provided to give the context. The entire DoDs maps are presented in Figure 6 of the Supplementary Materials section.

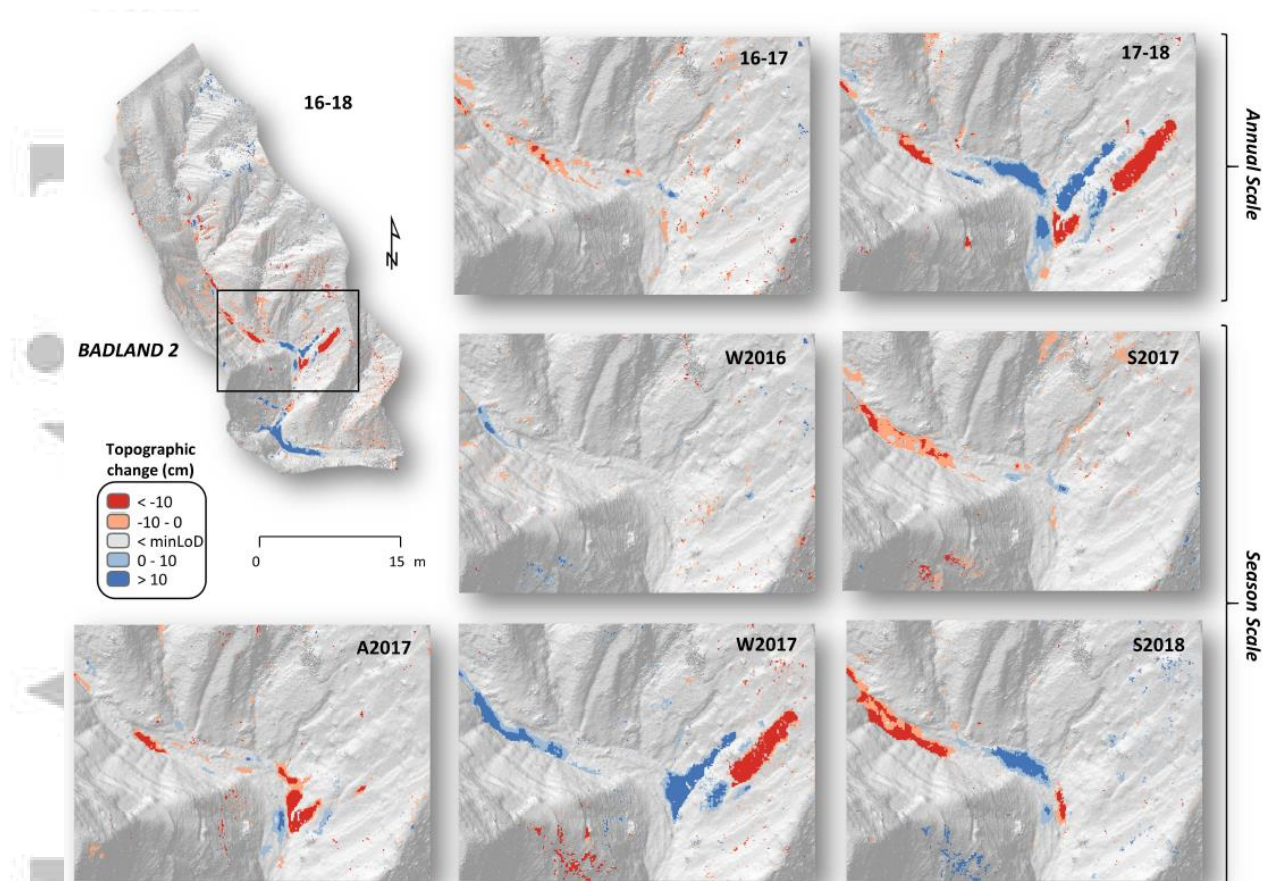


Figure 5. DoD maps of a representative area of B2 for the different analysed temporal scales: annual (upper part) and seasonal (lower part) scales. Note that the DoD of the entire badland (top left) corresponds to the map associated with the complete study period (2016-2018) in this badland. The location of the representative area is also shown. Changes below the minLoD are not presented (considered uncertain) and an underlying shaded DEM is provided to give the context. The entire DoDs maps are presented in Figure 7 of the Supplementary Materials section.

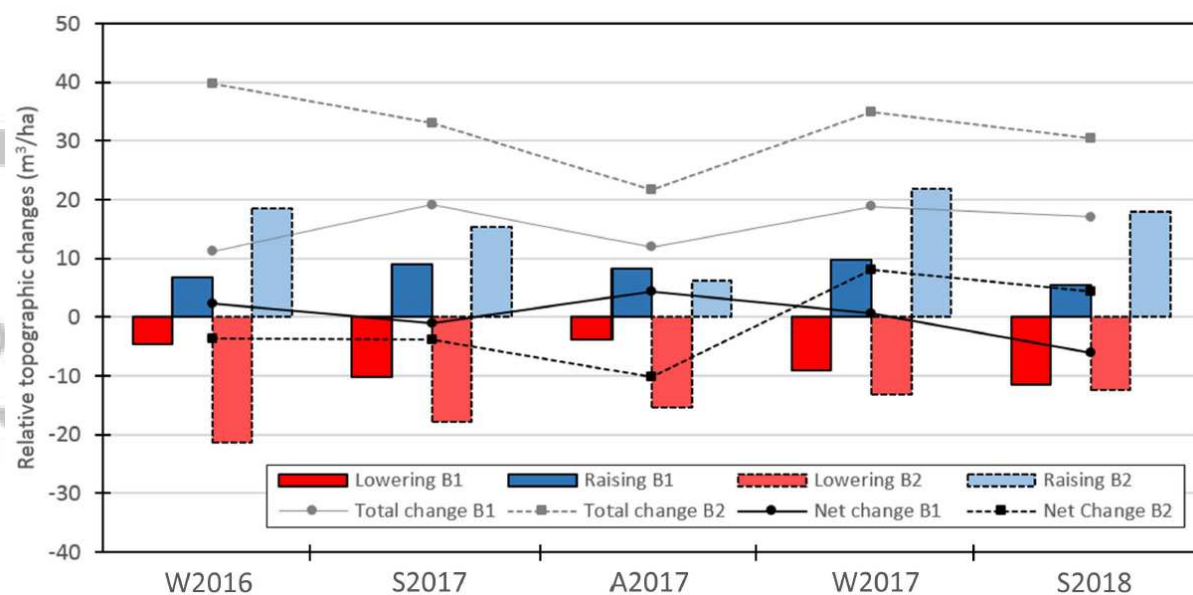


Figure 6. Specific topographic changes (expressed as $\text{m}^3 \text{ha}^{-1}$) in both badlands for the period 2016-2018 (the fully coincident period between B1 and B2). Total lowering (red columns), total raising (blue columns), total topographic change (grey lines) and net topographic change (black lines) are presented. Lines correspond to B1, while dotted lines correspond to B2.

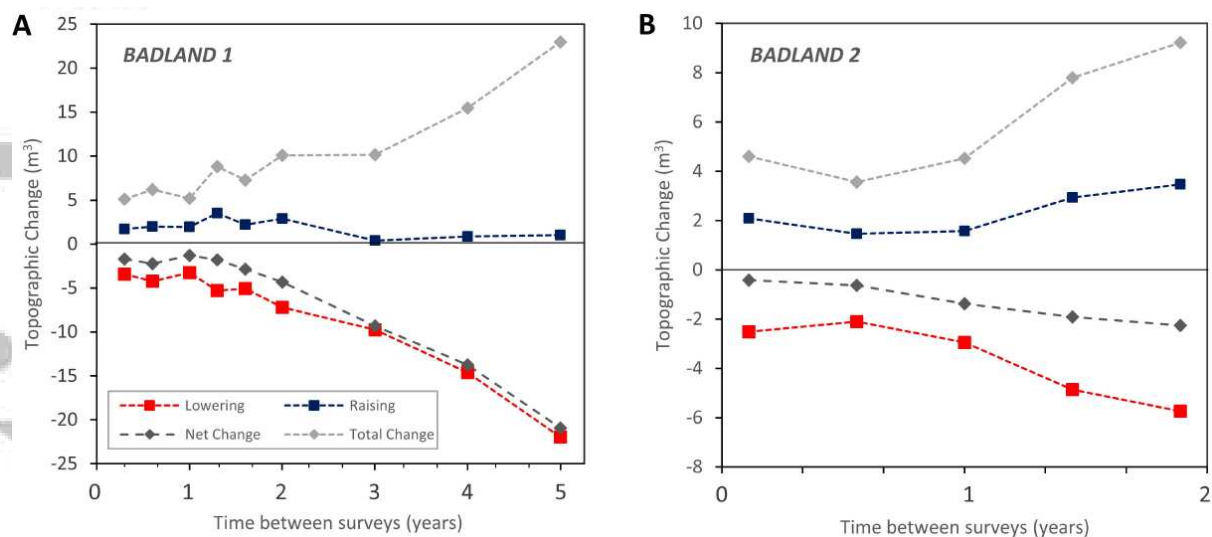


Figure 7. Evolution of volumetric topographic changes (i.e. lowering, raising, total change and net change) for different temporal scales in (A) B1 and (B) B2 B). Note that the legend only appears in A but remains the same for B.

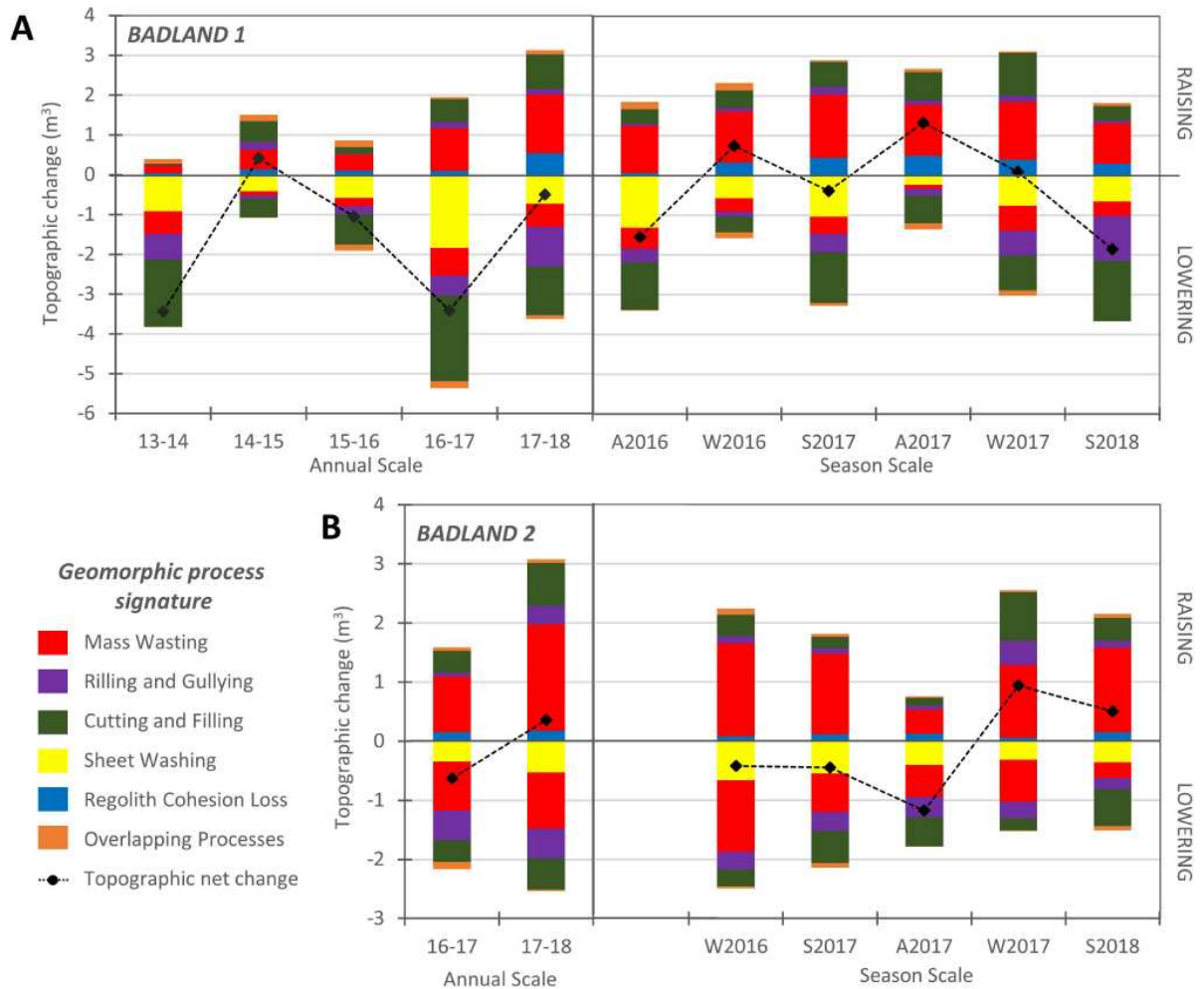


Figure 8. Volumetric changes associated to geomorphic processes obtained from the MaGPiE algorithm for both (A) B1 and (B2) experimental badlands and at the different temporal scales analysed (i.e. annual and seasonal). The net topographic change is also presented with a dotted black line for all the periods.

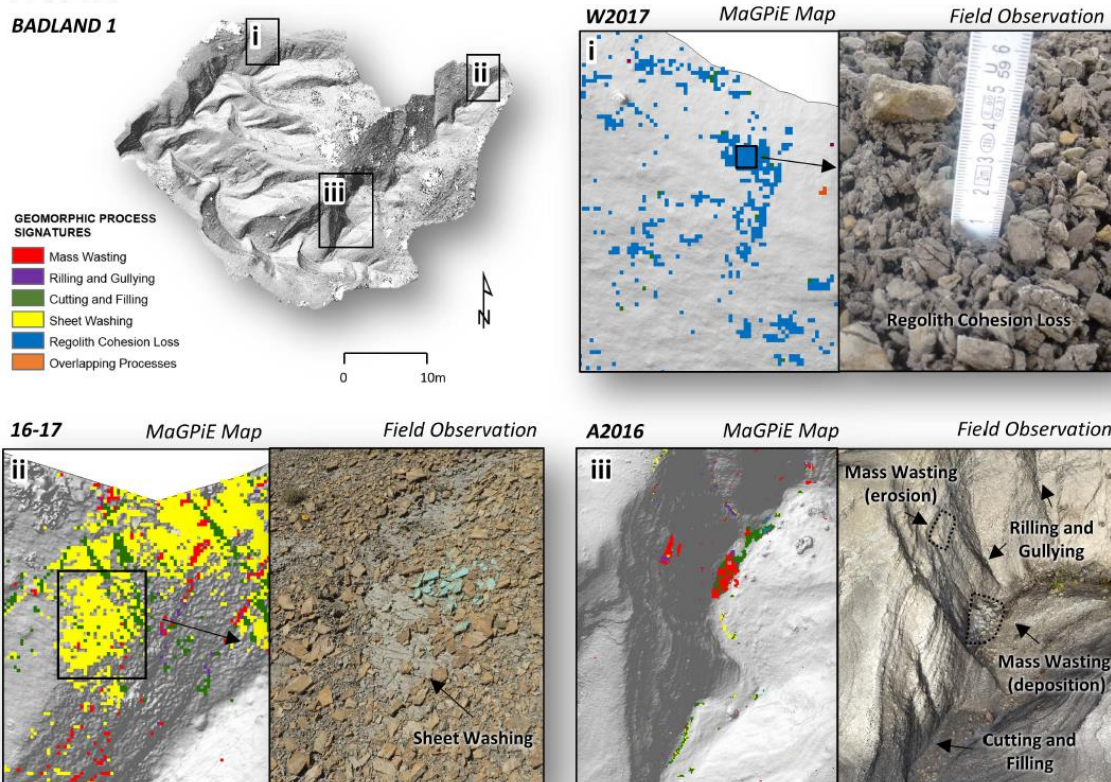


Figure 9. Examples of geomorphic maps of processes linked to field observations for different periods in some specific areas of B1. Note that the entire maps are presented in Figure 9 of the Supplementary Materials section.

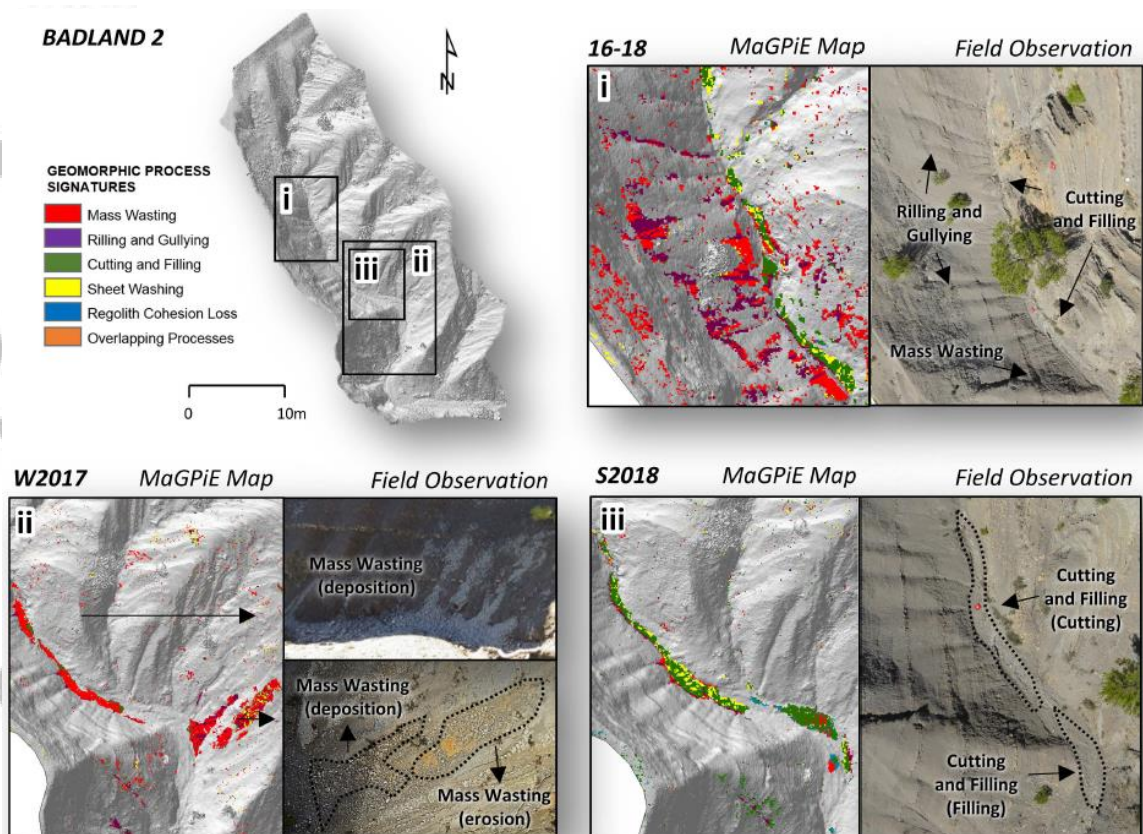


Figure 10. Examples of geomorphic processes maps linked to field observations for different periods in some specific areas of B2. Note that the entire maps are presented in Figure 10 of the Supplementary Materials section.